npj | heritage science

Article

https://doi.org/10.1038/s40494-025-02061-7

Crack propagation risk threshold of classical garden rockeries based on LEFM

Check for updates

Ziwen He[1], Xiaodong Zhang[2], Li Fu[1], Yufan Ho[1], Qianting Huang[1] & Qingping Zhang[1]

Traditional Chinese garden rockeries, exposed to long-term weathering and human activities, often suffer structural deterioration. However, crack propagation risks in these heritage structures have not been numerically analyzed. This study investigates the structural crack propagation risk threshold of rockeries using numerical simulation. A damage survey and data collection were conducted on the Small-rock Mountain Adobe of He Garden in Yangzhou, resulting in a structural crack database and finite element model. Static analysis assessed crack damage and identified primary deterioration causes. Linear elastic fracture mechanics (LEFM) was then used to predict crack initiation and propagation in intact rocks, with outcomes cross-validated against observed damage. Critical propagation paths of major cracks were forecasted at different stages. Finally, crack risk levels were determined using the stress intensity factor, and thresholds for crack growth were obtained, including the corresponding critical crack size and vertical displacement, providing a basis for conservation strategies.

Classical Chinese gardens are treasures of the world's cultural heritage and represent the artistic culmination of ancient Chinese civilization. The classical Gardens of Jiangnan are typical representatives of these gardens, showcasing the pinnacles of ancient Chinese garden construction techniques. As key features of these gardens, rockeries hold immense historical and artistic value, forming the centerpiece of many heritage sites. As many traditional Chinese garden rockeries are located outdoors, long-term exposure to natural and anthropogenic factors leads to an increasing incidence of structural deterioration[1]. Cases such as the collapse of the rockery in Suzhou's Garden of Pleasure, the progressive cracks near the south side of Jianshan Pavilion in the Lion Grove Garden, and the subsidence, displacement, structural fractures, and root-induced splitting in the Mountain Villa with Embracing Beauty indicate the urgent need for the structural protection of garden rockeries.

Digital technologies such as terrestrial scanning (TLS)[2], handheld laser scanners[3], and digital photogrammetry have been widely used to model and measure the three-dimensional morphology of rockery structures and individual boulders. Dong et al.[4] explored digital modeling and 3D printing of classical Chinese garden rockeries. Wang et al.[5] improved the accuracy and efficiency of rockery design using material digitization. Wang et al.[6] investigated volume calculation methods for irregular stone cultural relics. In these studies, the relevance of 3D modeling in the intersection of cultural heritage preservation and structural surveying is particularly demonstrated[7]. These advancements provide the foundation for constructing finite element models (FEMs) of cultural heritage rockeries, facilitating further research on crack development.

Numerical simulations for analyzing damage in brick-and-stone cultural heritage structures have gradually become more systematic[8]. These simulations are commonly used to infer structural damage causes or simulate the damage conditions of large natural-disaster-prone cultural heritage sites[9,10]. Advanced numerical methods are critical in linking observed damage with its causes, enabling the design of minimal yet sufficient reinforcement strategies[11], particularly through inverse problems[12]. Extensive studies have been conducted on the local settlement of foundations[13–15] and FEM simulations have been employed to monitor and assess the long-term stability of such structures[16,17]. For example, the preliminary construction of a preventive protection system for the cliffs of Mogao Grottoes in Dunhuang included protection state assessments, numerical simulations, and protection monitoring[18].

In the analysis of structural deterioration in rockeries, Dong et al.[19] used FEM analysis to examine the stability of the stacking process in rockeries. Zhang et al.[20] identified stress concentration areas in rockery cultural heritage sites under self-weight and tourists loads through FEM analysis, thereby determining key monitoring zones to support preventive conservation efforts. Fu et al.[21] performed risk assessments of rock garden structures based on physical fragility indices derived from finite-element simulations.

However, most research on crack propagation in cultural heritage sites has focused on the structural stability risks caused by dynamic environmental changes, such as earthquakes[22–25], and structural stability safety

[1]College of Landscape Architecture, Nanjing Forestry University, Nanjing, Jiangsu, China. [2]Administrative Committee of Jiangsu Gaochun Economic Development Zone, Nanjing, Jiangsu, China. e-mail: qpzh@njfu.edu.cn

assessment methods for crack propagation in cultural heritage[26,27]. To date, no numerical simulation analyses of structural crack propagation risk in classical garden rockeries have been reported. Therefore, this study investigates the structural crack propagation risk threshold in cultural heritage rockeries using numerical simulation.

Predicting crack growth in rock heritage sites using numerical simulations is challenging and requires specific modeling and analysis strategies[11]. Rock fracture mechanics offers a robust theoretical framework. Based on the loading conditions, cracks are classified into three fundamental modes:

Mode I: Cracking mode—the crack spreads along the surface normal.

Mode II: Shear mode—the crack propagates along the shear direction.

Mode III: Torsional mode—the crack propagates in the torsional direction[28].

Although loading conditions in rock engineering often involve combined fracture modes, the relatively low tensile strength of rock makes Mode I the most prevalent. Notably, even composite fracture scenarios are often simplified to Mode I conditions, with fracture assumed to occur when the equivalent stress intensity factor reaches the Mode I fracture toughness, K_{IC}.

The classical garden rockery examined in this study is a lake stone rockery composed of limestone. Limestone exhibits a typical brittle fracture behavior during tensile loading. Linear elastic fracture mechanics (LEFM) theory, adopted to model crack propagation, assuming a linear relationship between stress and strain until plastic deformation occurs, is effective for modeling brittle rock failure[29]. The stress-intensity factor solution obtained from LEFM can be used to evaluate crack propagation[30]. The criteria for determining the crack propagation direction include: (1) maximum energy release rate criteria, (2) maximum circumferential stress criterion or maximum principal stress criterion, and (3) minimum strain energy density criterion. The maximum principal stress criterion[31,32] was adopted in this study, as damage initiation starts when the maximum principal stress at a point exceeds the tensile strength of the material. Crack propagation follows a linear evolution model based on the energy release rate, propagating in the direction that maximizes the total energy release.

Although significant progress has been made in understanding the structural stability of rockeries, a numerical simulation framework to evaluate crack growth risks based on fracture mechanics remains underdeveloped. This study further builds on the theoretical foundation of LEFM to simulate crack growth risk in classical rockery structures.

In particular, this study investigates the risk threshold for crack development. Figure 1 illustrates the research methodology, which includes the following steps. First, a structural crack database is established, and 3D point cloud information of the rockery structure is collected and processed. Second, crack damage is assessed, and the primary causes of deterioration are identified through static analysis, leading to the development of a preliminary damage diagnosis report. Third, using Abaqus software and the LEFM method, the cracking mode and crack propagation path of the rockery were numerically simulated. Finally, crack propagation risk levels for the most critical defects were evaluated, and corresponding critical crack sizes and vertical displacement values were identified as the risk threshold. The results provide a robust numerical simulation framework for quantifying crack propagation risks and offer an objective basis for the preventive protection of classical garden rockeries.

Methods

Preprocessing of finite element analysis of the stability of the rockery structure

Damage survey. Historical information and relevant literature were investigated to determine the historical context, including damage and repair status since the garden's establishment. Data collection was performed using TLS[33], handheld scanners, and other digital techniques to capture 3D data of the rockery for dynamic monitoring and model reconstruction. A field damage survey was conducted to obtain present structural damage information on structural cracks, such as length, width, depth, location, and crack orientation, and to make preliminary inferences on the leading causes of the damage. Each crack was numbered, and the compiled crack data were used to establish a structural damage database, which was updated continuously throughout the monitoring period.

Point cloud model preprocessing. The original point cloud data is imported into Trimble RealWorks for preprocessing. As the measured point cloud data contains coordinates, data from each site can be automatically combined using the "Auto-register using Planes" mode. For data that cannot be automatically recognized and combined, manual alignment is performed using the "Cloud-Based Registration" mode. Refined error values and overlap rates are used as registration criteria, resulting in complete point cloud data obtained through scanning. Due to the complex surrounding environment—including vegetation, buildings, water features, and roads—as well as surface impurities such as moss and shrubs, the original point cloud of the rockery may be incomplete or may not fully represent its true surface[3]. Although Trimble RealWorks includes a point cloud classification function, the intricacy of the classical garden environment and the frequent overlap of various features necessitate manual removal of redundant data to produce complete, clean, and independent point cloud data of the rockery[20]. Subsequently, the point cloud is sampled in Trimble RealWorks at an appropriate proportion, and the triangulation surface model is created using the surface fitting tool. At this stage, the generated rockery model is incomplete, and pores appear in localized areas. To address this, the automatically generated triangular surface model file is imported into Geomagic Wrap software for further refinement, and the hole repair tool is used to repair the pores individually. After preliminary processing, the model is checked using Mesh Doctor and redefined to produce a more regular triangular mesh model.

Model topological simplification. Owing to the structural complexity of rockeries and the high precision of scanning devices, the initial mesh typically contained many elements, rendering finite element modeling computationally intensive. Therefore, mesh simplification was necessary to reduce the number of elements while preserving structural characteristics[34].

Voxel finite element model preparation for simulation: For irregular geometric bodies such as rockeries, remeshing in ABAQUS is challenging. Therefore, voxelization was chosen as a meshing strategy. This approach retained key surface features while improving meshing efficiency[35]. The voxelized model was created with appropriate spacing to balance geometric fidelity and computational performance. The model was subsequently imported into Abaqus, using C3D8R elements.

Static analysis and damage diagnosis

Static analysis was conducted on the finite element model to obtain stress weakness under the present conditions, and a comparison was made with the difference in structural crack data and historical point cloud data obtained from the field investigation[36] to verify and reverse deduce the leading causes of structural deterioration in the rockery.

Based on the field survey results, a comparison of historical point cloud data, and static analysis results from numerical simulations, the data were processed for visualization to generate a preliminary damage diagnosis report for rockery cracks.

Subsequently, a preventive and periodic monitoring plan was developed for each crack damage diagnosis report. For example, for cracks caused by local foundation settlement, a periodic comparison of historical point-cloud data[37] was conducted to monitor the changes and trends. Preventive measures were implemented at various risk levels. For cracks caused by stress concentration, visitor access to the rockery was adjusted according to the crack's risk level at different stages. Figure 2 summarizes the workflow of numerical simulation.

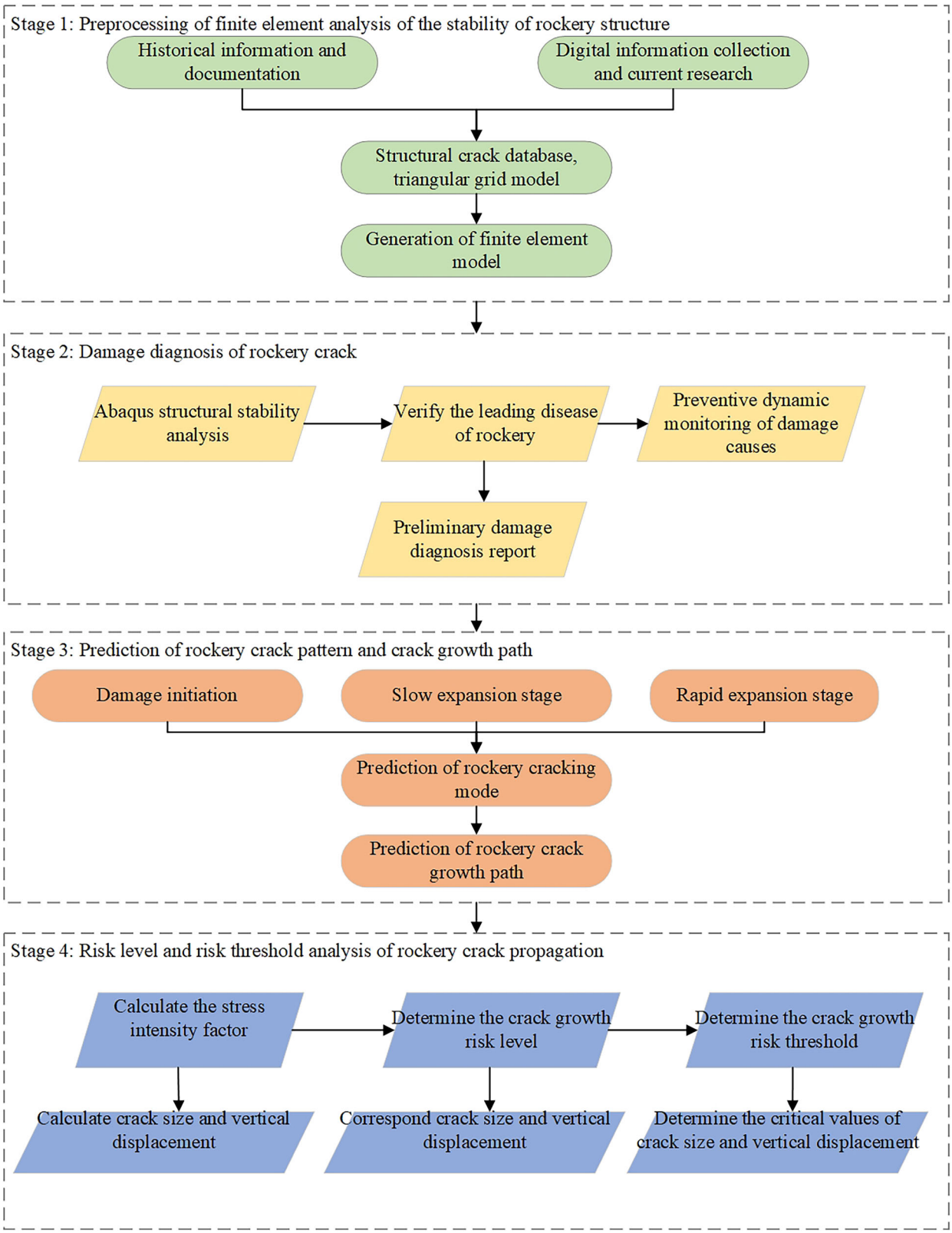

Fig. 1 | Flowchart illustrating the research method of the crack growth risk threshold.

Prediction of crack pattern and crack growth path

LEFM assumes a linear elastic response near crack tips and characterizes the stress field using the stress intensity factor (SIF). For Mode I loading, the SIF is defined as

$$K_I = \sigma\sqrt{\pi a} \tag{1}$$

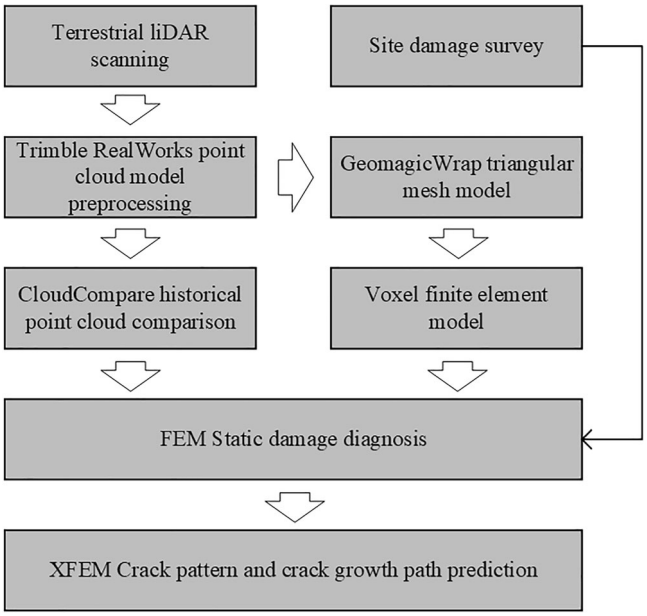

Fig. 2 | Numerical simulation workflow.

where σ is the applied stress and a is the crack length.

The maximum principal stress criterion is used as the criterion for crack initiation, which holds that the crack will occur when the maximum principal stress reaches the ultimate strength of the material. Material failure is assumed to occur when the maximum principal stress σ_{max} reaches the ultimate strength of the material σ_c, i.e.:

$$\sigma_{max} = \sigma_c \tag{2}$$

The energy release rate (G) describes the energy change during crack propagation. This represents the energy the system releases per unit of crack area expansion. For three-dimensional crack propagation, when the energy release rate G reaches the critical energy release rate G_c of the material, the crack continues to expand,

$$G = G_C \tag{3}$$

The relationship between energy release rate and SIF is as follows:

$$G = \frac{K_I^2}{E} \tag{4}$$

where G is the energy release rate, K_I is the SIF of Mode I, and E is the Young's modulus of the material.

Finally, the risk level of rockery crack propagation is assessed using the ratio:

$$R = \frac{K_I}{K_{IC}} \tag{5}$$

where K_I is the SIF of Mode I and K_{Ic} is the fracture toughness of limestone. Based on the value of R, crack propagation risk is categorized into three levels:

Level I (Low Risk): $0 < R < 1.0$, crack size remains stable initially, followed by damage initiation.

Level II (Moderate Risk): $1.0 \le R < 2.0$, crack size expands at a relatively stable rate.

Level III (High Risk): $R \ge 2.0$, crack size increases rapidly until instability and failure.

Table 1 | Material parameters of limestone

Material parameters	Symbol	Data	Unit
Young's modulus	E	7.50E + 10	Pa
Poisson's ratio	v	0.32	/
Density	ρ	2700	kg/m^3
Energy release rate	G	30	J/m^2
Tensile strength	σ_t	2.00E + 06	Pa
Inherent fracture toughness	K_{IC}	1.50E + 06	Pa·m$^{0.5}$

Corresponding critical crack sizes and vertical displacement values for each risk level were determined as the risk threshold.

Therefore, by calculating the SIF K_I and comparing it with the inherent fracture toughness K_{IC} of limestone, this metric serves as a key basis for assessing the risk level of crack propagation in artificial rockeries. To simulate this process efficiently, the extended finite element method (XFEM) is employed, as it can simulate crack propagation without remeshing. Therefore, it is particularly suitable for three-dimensional crack simulation in complex structures.

To implement this method, a voxel-based finite element model in C3D8R format was imported into the ABAQUS simulation platform. The limestone material was defined as an isotropic elastic model with a Young's modulus of 7.5×10^{10} Pa, Poisson's ratio of 0.32, and density of 2700 kg/m^3. The crack initiation criterion followed the maximum principal stress criterion, and the maximum principal stress was 2×10^6 Pa. Crack propagation was modeled using an energy-based damage evolution model with $G_{IC} = G_{IIC} = G_{IIIC} = 30$ N/m^2, and $\alpha = 1$. The extended finite element method (XFEM) was adopted for crack development, and the entire rockery process from crack initiation to crack penetration was observed without prefabrication for crack mode prediction. The crack with the highest risk was prefabricated in the crack growth prediction, and its crack growth path was observed. Boundary conditions included full constraint of the rockery base (ENCASTRE U1 = U2 = U3 = UR1 = UR2 = UR3 = 0), the vertical displacement (U3 = −0.12 m) is set in the settlement area, and the rockery is subject to self-weight load (−9.8 N/m^2) as a whole. The SIF of the output crack tip was set in the historical output module of the analysis step.

The specific material parameters of limestone are shown in Table 1. Based on existing research on numerical simulation of cultural heritage rockeries[21], particularly the review by Zhang et al.[20], who reviewed the literature and compared various mechanical parameters through simulation, the performance parameters of typical rockery stone materials were determined. It was confirmed that, under identical loading and structural conditions, variations within the parameter range of rock materials had a relatively minor impact on computational outcomes. Therefore, in this study, limestone mechanical parameters, such as density, Poisson's ratio, elastic modulus, and tensile strength, were selected with reference to these prior studies. Numerical simulations were also conducted on materials with varying typical energy release rate values ranging from 20 to 50 J/m^2[38], and the force–displacement curves of crack propagation showed consistent behavior within this range. Accordingly, a moderate energy release rate value of 30 J/m^2 was selected as the representative value, from which the corresponding fracture toughness ($K_{IC} = 1.5$ MPa·m$^{0.5}$)[39–41] was derived using the relation as follows:

$$K_{IC} = \sqrt{G_C E} \tag{6}$$

Research area

He Garden, located at 66 Xu Ning Men Street, Guangling District, Yangzhou City, Jiangsu Province, China (Originally named "Jixiao Villa)," was founded in the mid-Qing Dynasty by the Provincial Administrator, He

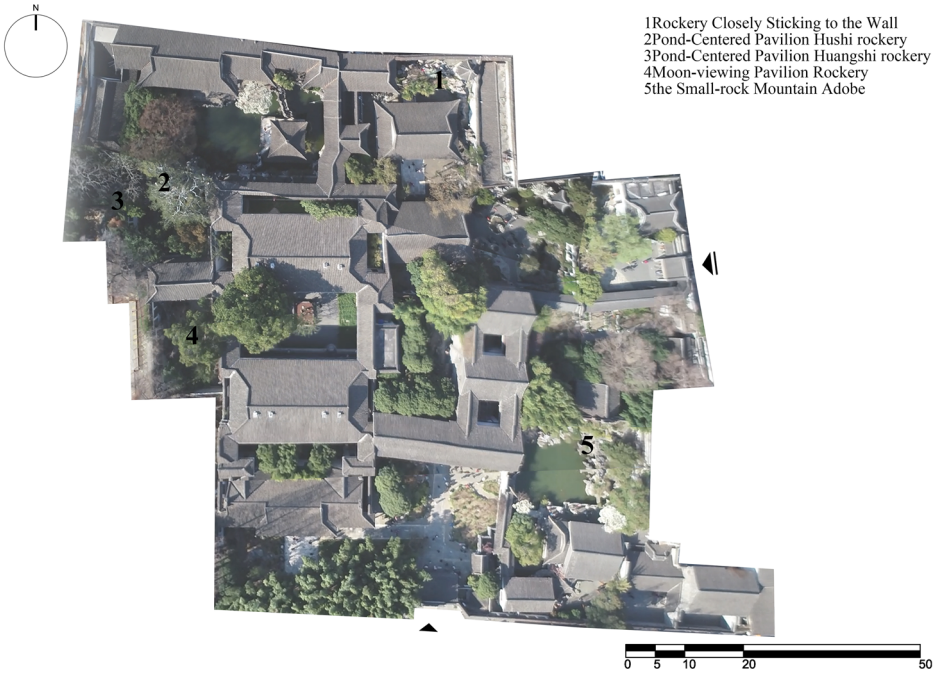

Fig. 3 | He Garden plan and the location of the Small-rock Mountain Adobe.

Zhile. In 1988, the State Council designated He Garden as a Major Historical and Cultural Site Protected at the National Level, and in 2007, it was included in the first batch of "National Key Parks" along with the Summer Palace in Beijing and 20 other gardens. He Garden is one of Yangzhou's best preserved and most representative gardens. It was also praised as the "First Garden of the Late Qing Dynasty."

Among its features, the small rock mountain, Adobe (Pian Shi Shan Fang), was rebuilt in the 1980s. Due to many years of neglect, significant sections of the rockeries collapsed and were damaged, leading to restoration work in 1989. After the restoration, the rockery was designed based on the stone-stacking method from the works of artist Shi Tao, with the main peak to the west and supporting peaks to the east[42]. The original appearance of the stone house at the base of the main peak and the cave at the eastern end was retained. The stone-stacking technique and the color and pattern of the stones on the eastern side harmonized with the natural landscape, respecting the original layout while expanding the pond. This study analyzed rocks in the Small-Rock Mountain Adobe of the He Garden. According to a preliminary report of the structural damage investigation of the rockery, the cave area in the middle of the rockery was significantly affected by the local settlement of the foundation. Figure 3 shows He Garden plan and the locations of five rockeries.

Damage survey

A Trimble RealWorks ground-based 3D laser scanner collected point cloud data for He Garden in Yangzhou. A point-cloud scan was conducted in September 2021, followed by a second scan in January 2025.

The actual crack patterns in the rockery were primarily identified through a visual damage survey[43] and classifications of structural damage causes identified[1]. After the initial investigation, 14 structural cracks were found in the Small-rock Mountain Adobe rockery, two likely caused by foundation settlement. These cracks were located near the revetment area. The rock base was affected by local revetment settlement, resulting in structural cracks. Twelve cracks were caused by stress-induced fissures, two by adhesive detachment, and one by plant-root splitting. Several cracks were caused by a combination of multiple structural damage mechanisms. Figure 4 shows the Small-rock Mountain Adobe zoning diagram.

Building on Fu's classification of structural issues in Jiangnan Garden rockeries[1], this study presents a detailed categorization of the causes of structural crack-related damage, as shown in Table 2.

According to the classification method, the investigation results of structural crack damage of four rockeries in the Yangzhou He Garden cultural heritage site are summarized, as shown in Table 3. Among them, no obvious structural cracks were found in the Pond-Centered Pavilion Hushi rockery by on-site investigation, so it was not included in this table.

Results

Finite element model

Figure 5 shows an example of the model generation of small-rock mountain adobe (SRMA) from the point cloud to numerical modeling, including triangulation mesh fitting, triangular mesh modeling, and a topological simplification model to voxel model generation[44]. Specifically, the point cloud of the SRMA was first collected using Terrestrial LiDAR Scanning (Fig. 5a). Trimble RealWorks-Geomagic Wrap was used to perform triangular mesh pre-processing (Fig. 5b), mesh doctor repair (Fig. 5c), topological simplification model (Fig. 5d), and rock model partitioning (Fig. 5e). Finally, the "voxel model" of the west side cavern, the west main peak, the main peak east to central area, and the central cavern was obtained by using a $0.2 \times 0.2 \times 0.2$ (m) voxel model (Fig. 5f).

Model validation

Through static analysis, the maximum principal stress, maximum principal strain, and distribution position of the SRMA rockery were obtained and compared with the status of the structural cracks in the rockery obtained from the damage investigation. The main cause of the structural cracks in each SRMA zone was verified and used as an important reference for long-term dynamic monitoring and further simulation of the SRMA rockery cracking mode and crack growth path.

The mechanical behavior of the western zone under self-weight load was analyzed through numerical simulation, as shown in Fig. 6.

The mechanical behavior of the central cavern under self-weight load and local settlement of the foundation was analyzed through numerical simulation, as shown in Fig. 7.

The mechanical behavior of the main peak east to central area under self-weight load was analyzed through numerical simulation, as shown in Fig. 8.

The maximum principal stress, maximum principal strain, and distribution of each zone of the SRMA rockery are summarized in Table 4.

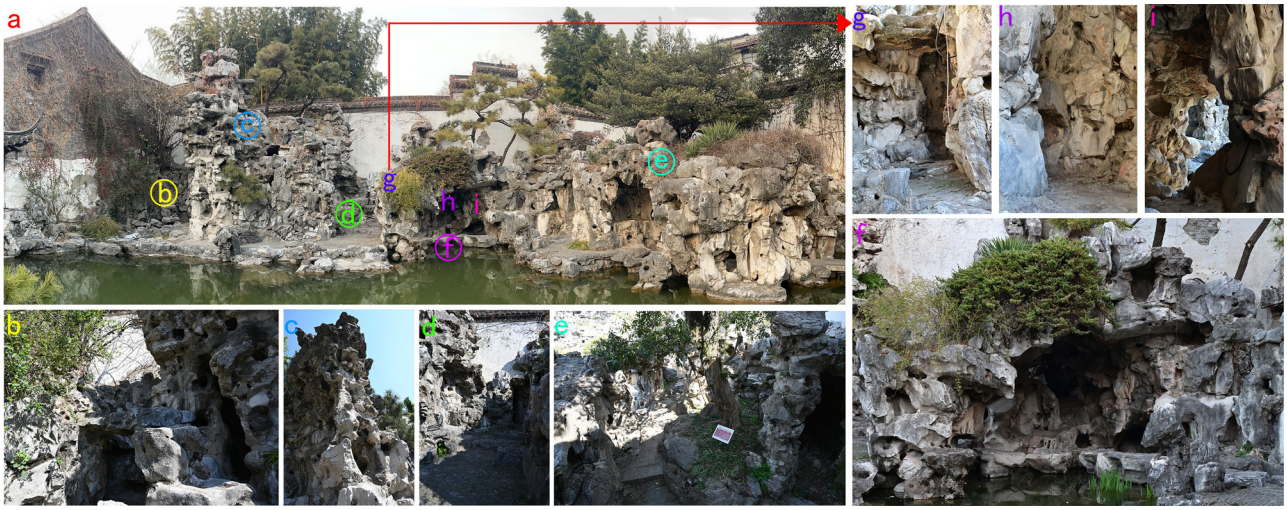

Fig. 4 | Small-rock Mountain Adobe zoning diagram. **a** Panoramic view, **b** West side cavern, **c** West main peak, **d** Main peak east to central area, **e** East side area, **f** Central cavern, **g** Central cavern entrance, **h** Central cavern corner, and **i** Central cavern exit).

Table 2 | Classification of the causes of structural crack-related damage

Damage causes	Damage characterization
A. Foundation settlement	Rockery sinks or shifts under the action of gravity as a whole
B. Peak rock tilt	The false mountain rock inclines and displaces due to external forces
C. Adhesive detachment	Powder off: The adhesive powder between the rockery stone body is peeled off
	Whole piece off: The adhesive between the rockery stone body is broken off
D. Stress crack	The partial stone structure of the rockery is cracked and the depth is deep
E. Plant–root splitting	Plants grow in the gap between rockeries and destroy rockeries through root splitting, resulting in cracking of rockeries

Preliminary damage diagnosis report of the Small Rock Mountain Adobe

The static simulation results for each area of the SRMA rockery were compared with the structural crack trend obtained from the on-site damage survey. The results are summarized in Table 5, including the crack number, maximum principal stress diagram, maximum principal strain diagram, and current crack trend diagram.

The primary causes of deterioration of the 14 structural cracks were identified through the damage diagnosis of the SRMA rockery. The results are summarized in Table 6, including crack number, length, width, depth, and the leading causes of each crack. Through the diagnosis of structural cracks in the central cavern, the approximate area of local settlement in the rockery foundation was determined, along with the corresponding interaction relationship settings in Abaqus (Fig. 9).

Prediction of central cavern cracking mode

In 2021, the main damage in the central cave area of the SRMA was caused by the local settlement of the foundation, and the cracking mode of the central cave area of the SRMA under the local settlement of the foundation was numerically simulated using the XFEM in ABAQUS (Fig. 10).

Table 7 lists specific information on the starting point, ending point, and important nodes of each stage of the rockery cracking mode. In the crack model prediction of the middle chamber region of the SRMA in 2021, the crack initiation location and expansion path were consistent with crack number 3.6. The crack size was also the largest. Therefore, this crack was used for further numerical simulation of the crack expansion path.

The current investigation of the crack status of the central cavern rock is consistent with the (c) and (d) stage of the slow crack expansion in the crack prediction simulation (Fig. 11).

Risk threshold and risk level classification

Using the XFEM of Abaqus, the SIF of crack No. 3.6 was calculated, and K_I/K_{IC} (R) was obtained to classify the crack risk level. The corresponding maximum vertical displacement of special points, crack volume, and crack area were summarized, as shown in Table 8.

To ensure the rationality of the risk grade classification, the linear relationship between the steps, crack area, and crack volume was further verified by observation. In particular, when observing the relationship between the analysis step and crack volume change, the crack size change was gentle from Stage I to II; the crack size then significantly accelerated in Stage III (Fig. 12).

To establish a quantitative basis for risk assessment, the thresholds for crack growth were defined based on critical crack sizes and vertical displacements corresponding to each risk level. These thresholds are detailed in Table 9.

Prediction of crack growth path in the central cavern

The evolution of crack development was visualized at each stage of the simulation to capture the initiation, propagation, and final failure process, as shown in Fig. 13.

The evolution of the overall vertical displacement was visualized at successive simulation stages to illustrate the progressive settlement behavior of the structure, as shown in Fig. 14.

Six special points (P1–P6) were selected in the settlement area of the central cavern to observe the vertical displacement changes of

Table 3 | The investigation results of structural crack damage of four rockeries in He Garden cultural heritage site

Rockery name			1. Pond-centered pavilion Huangshi rockery				
Crack number	Rock crack picture	Crack direction	Crack location	Length (cm)	Width (mm)	Depth (mm)	Damage causes
1.1			Base on the west side of the middle tree pond	175	4.38	23.9	C
1.2			Middle base on the east side of the tree pond	109	1.36	/	C
1.3			Base on the west side of the middle tree pond	59	/	/	C
1.4			Base on the west side of the tree pool	100	/	/	E
1.5			Base on the west side of the tree pool	26	/	/	E
1.6			Base on the west side of the tree pool	122	/	/	E
1.7			Base on the middle tree pool	185	/	/	E

Table 3 (continued) | The investigation results of structural crack damage of four rockeries in He Garden cultural heritage site

Rockery name			1. Pond-centered pavilion Huangshi rockery				
Crack number	Rock crack picture	Crack direction	Crack location	Length (cm)	Width (mm)	Depth (mm)	Damage causes
1.8			Base on the middle tree pool	136	/	/	E
1.9			Base on the middle tree pool	121	/	/	E
1.1			Cave entrance on the west side	157	/	/	C
1.11			Cave entrance on the west side	117	/	/	C
1.12			Cave entrance on the west side	113	/	/	C
1.13			Cave entrance on the west side	93	/	/	C
1.14	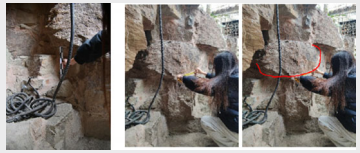		Cave entrance on the west side	130	/	/	C
1.15	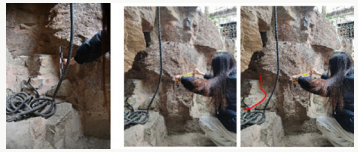		Cave entrance on the west side	50	/	/	C

https://doi.org/10.1038/s40494-025-02061-7

Table 3 (continued) | The investigation results of structural crack damage of four rockeries in He Garden cultural heritage site

Rockery name			1. Pond-centered pavilion Huangshi rockery				
Crack number	Rock crack picture	Crack direction	Crack location	Length (cm)	Width (mm)	Depth (mm)	Damage causes
1.16			Cave entrance on the west side	185	3.3	24.71	C
1.17			Middle base on the east side of the tree pond	80	4.2	52.49	C
1.18			Back of the middle tree pool	77	9.11	77.19	E
1.19			Cave wall	16	2.41	92.84	D
1.2			Cave wall	11	/	1.3	D
1.21			Huangshi rockery and lake rockery joint base	61	/	/	D
Rockery name			**2. Rockery closely sticking to the wall**				
Crack number	Rock crack	Crack direction	Crack location	Length (cm)	Width (mm)	Depth (mm)	Damage causes
2.1			Near the Jinyue pavilion platform to the lower steps	94	2.4	18	A

https://doi.org/10.1038/s40494-025-02061-7

Table 3 (continued) | The investigation results of structural crack damage of four rockeries in He Garden cultural heritage site

Rockery name			1. Pond-centered pavilion Huangshi rockery				
Crack number	Rock crack picture	Crack direction	Crack location	Length (cm)	Width (mm)	Depth (mm)	Damage causes
2.2			Steps of the west side corridor entrance	66	10.31	138.61	D
2.3	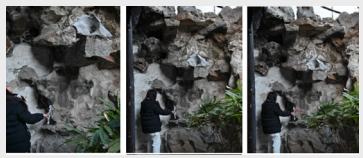		Pedestal of the Double-Path Cloister entrance	20	8.88	48.42	D
2.4			East side of the bottom cave	/	13.67	/	B
2.5			The inner corner of the east side of the rockery to the north side of the rockery	25	3.33	10.47	D
2.6			Near the Jinyue pavilion lower side steps	25	5.47	11.69	A
Rockery name			**3. Small-rock mountain adobe**				
Crack number	**Rock crack**	**Crack direction**	**Crack location**	**Length (cm)**	**Width (mm)**	**Depth (mm)**	**Damage causes**
3.1			Middle of the entrance pillar of the west-side cavern	92	10.48	90.58	CD
3.2			Middle of the roof of the west-side cavern	46	4.24	57.81	D

https://doi.org/10.1038/s40494-025-02061-7

Table 3 (continued) | The investigation results of structural crack damage of four rockeries in He Garden cultural heritage site

Rockery name			1. Pond-centered pavilion Huangshi rockery				
Crack number	Rock crack picture	Crack direction	Crack location	Length (cm)	Width (mm)	Depth (mm)	Damage causes
3.3			South side roof of the west-side cavern	51	2.41	18.88	D
3.4			Top of the central cavern	10.5	3.65	14.89	D
3.5			Top of the west entrance of the central cavern	61	/	31.51	D
3.6			Corner of the central cavern	100	3.94	54.79	A
3.7			West side of the main peak	35	4.76	31.16	CD
3.8			Western area near the courtyard wall	/	/	/	E
3.9			The top of a water-facing rock cave in the central cavern area	60	/	/	D

https://doi.org/10.1038/s40494-025-02061-7

Table 3 (continued) | The investigation results of structural crack damage of four rockeries in He Garden cultural heritage site

Rockery name			1. Pond-centered pavilion Huangshi rockery				
Crack number	Rock crack picture	Crack direction	Crack location	Length (cm)	Width (mm)	Depth (mm)	Damage causes
3.1			West base of the main peak	39	2.2	27.57	D
3.11	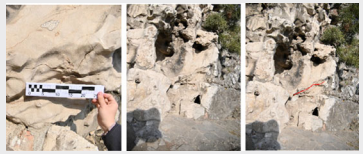		East base of the main peak	80	2.2	0.94	AD
3.12			Main peak east to central cavern	48	/	/	D
3.13			East of the central cavern door	7	2.74	4.58	D
3.14			Base of the rock at the summit of the main peak	/	/	/	BD
Rockery name			**4. Moon-viewing pavilion rockery**				
Crack number	**Rock crack**	**Crack direction**	**Crack location**	**Length (cm)**	**Width (mm)**	**Depth (mm)**	**Damage causes**
4.1			East side of the rockery in the west	26	2.66	6.77	D
4.2			Base of the south exit of the cave on the second floor	90	4.25	7.36	D

https://doi.org/10.1038/s40494-025-02061-7

Table 3 (continued) | The investigation results of structural crack damage of four rockeries in He Garden cultural heritage site

Rockery name			1. Pond-centered pavilion Huangshi rockery				
Crack number	Rock crack picture	Crack direction	Crack location	Length (cm)	Width (mm)	Depth (mm)	Damage causes
4.3			Base of the south exit of the cave on the second floor	28	2.67	5.89	D
4.4			Top of the aisle of the eastern rockery on the second floor	/	/	/	D
4.5			Base of the eastern rockery on the second floor	22	5	7.56	D
4.6			Top of the eastern rockery on the second floor	19	6.8	8.67	D
4.7			Between two rockeries in the middle of the first floor	/	5.72	8.17	D
4.8			Between two rockeries in the middle of the first floor	58	6.75	24	D
4.9			Base of the lower cave in the east	58	3.29	51.47	D
4.1			Steps to the second floor platform cave base	50	/	4.19	D

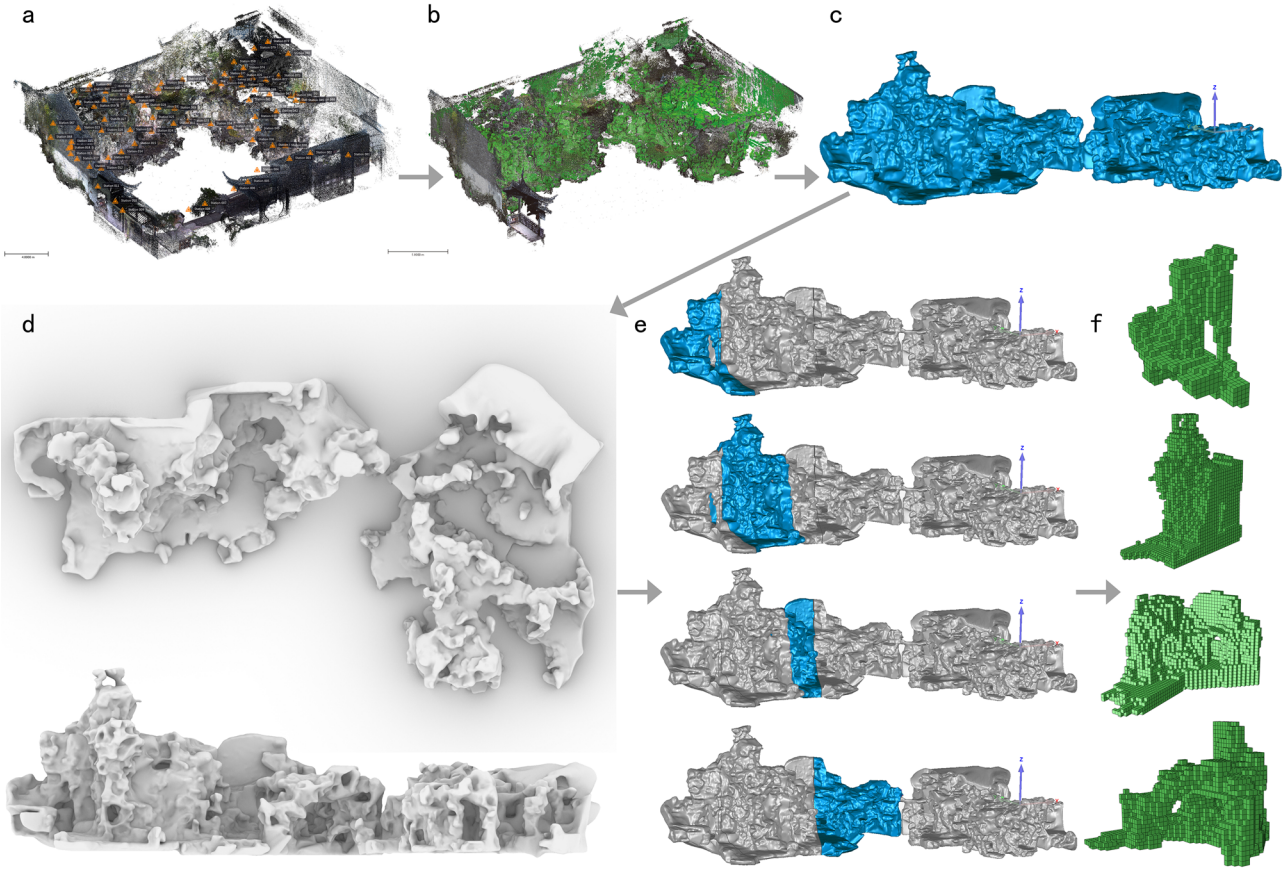

Fig. 5 | Workflow for generating the finite element model of the small-rock mountain adobe. a point cloud data collection, **b** triangular mesh pre-processing, **c** mesh doctor repair, **d** topological simplification model, **e** rock model partitioning, **f** voxel finite element model.

special points at each stage of the crack development process. A summary of the data is shown in Table 10, and a visual line chart is shown in the following Fig. 15.

Dynamic monitoring of crack growth in the central cavern

The following section compares the point cloud data of the SRMA from two scans conducted in 2021 and 2025, focusing on whether local settlement issues exist in the central cavern. Figure 16 shows the 3D scanning position.

The change data of the point cloud in the central cavern of the SRMA in 2021 and 2025 were compared using the CloudCompare software to analyze the revetment settlement trend. Using the plug-in M3C2 Distance in CloudCompare, the point cloud in 2021 was taken as the reference point cloud, and the point cloud data in 2025 was compared to form a comparative deformation map of the point cloud in 2025. If a subsidence area appears, it should be negative and can be used as a reference for determining the subsidence area of the central cavern of the SRMA (Fig. 17).

A comparison of the data from two ground-based laser scans conducted five years apart indicated that the regions with potential settlement were closely aligned with the damage diagnosis. However, owing to errors in point-cloud registration, further dynamic monitoring of the settlement phenomenon in this area is required, along with more detailed point-cloud difference comparisons at smaller scales.

Subsequent monitoring cycles can be scheduled annually.

Discussion

Injury diagnosis results: Because rockery has a long history and monitoring data before 2021 are missing, this study adopts the inverse inference method that links the damage status with the disease causes and deduces the leading disease causes of rockery cracks by combining historical literature information and the damage status. Figure 18 marks the specific locations of the 14 cracks of the SRMA.

Stress cracks mainly cause structural cracks in the western zone. According to the damage survey, the obvious structural cracks in the western zone of the SRMA are on the west side of the cavern roof and the pillar of the cave entrance, and the obvious structural cracks in the west main peak are concentrated on the two sides. According to the static analysis results, the maximum peak value of the principal stress was 1.99E + 05 Pa, which was located in the middle of the entrance pillar of the west-side cavern, ~1.5 m from the foundation. The maximum principal strain peak was 3.66E−06 Pa and was located on the west side of the main peak, west central, ~1.25 m from the foundation. In the field investigation of structural cracks in the western zone of the SRMA, there were three structural cracks numbered 3.1, 3.2, and 3.3, in the west side cavern, and two cracks numbered 3.7 and 3.10 in the western part of the main peak. There is a crack numbered 3.11 at the base of the eastern part of the main peak, and a crack numbered 3.14 at the base of the rock at the summit of the main peak, consistent with the stress concentration area in the static analysis results.

Stress cracks and local settlement of the foundation mainly cause structural cracks in the central cavern. According to field investigations, the central cavern has noticeable structural cracks, which are mainly located at the top of the central cavern and the corner of the interior wall. According to the investigation status of crack Nos. 3.4, 3.5, 3.9, and 3.13 structural cracks leading to diseases caused by stress concentration, the bottom of the rockery is completely constrained, subject to self-weight load static analysis and simulation. The main cause of crack No. 3.6 was inferred to be the local settlement of the foundation. Therefore, based on the crack location obtained from the current investigation, the displacement area of the rockery foundation was inferred, and the vertical displacement was set in the local settlement area of the foundation for the static analysis and simulation.

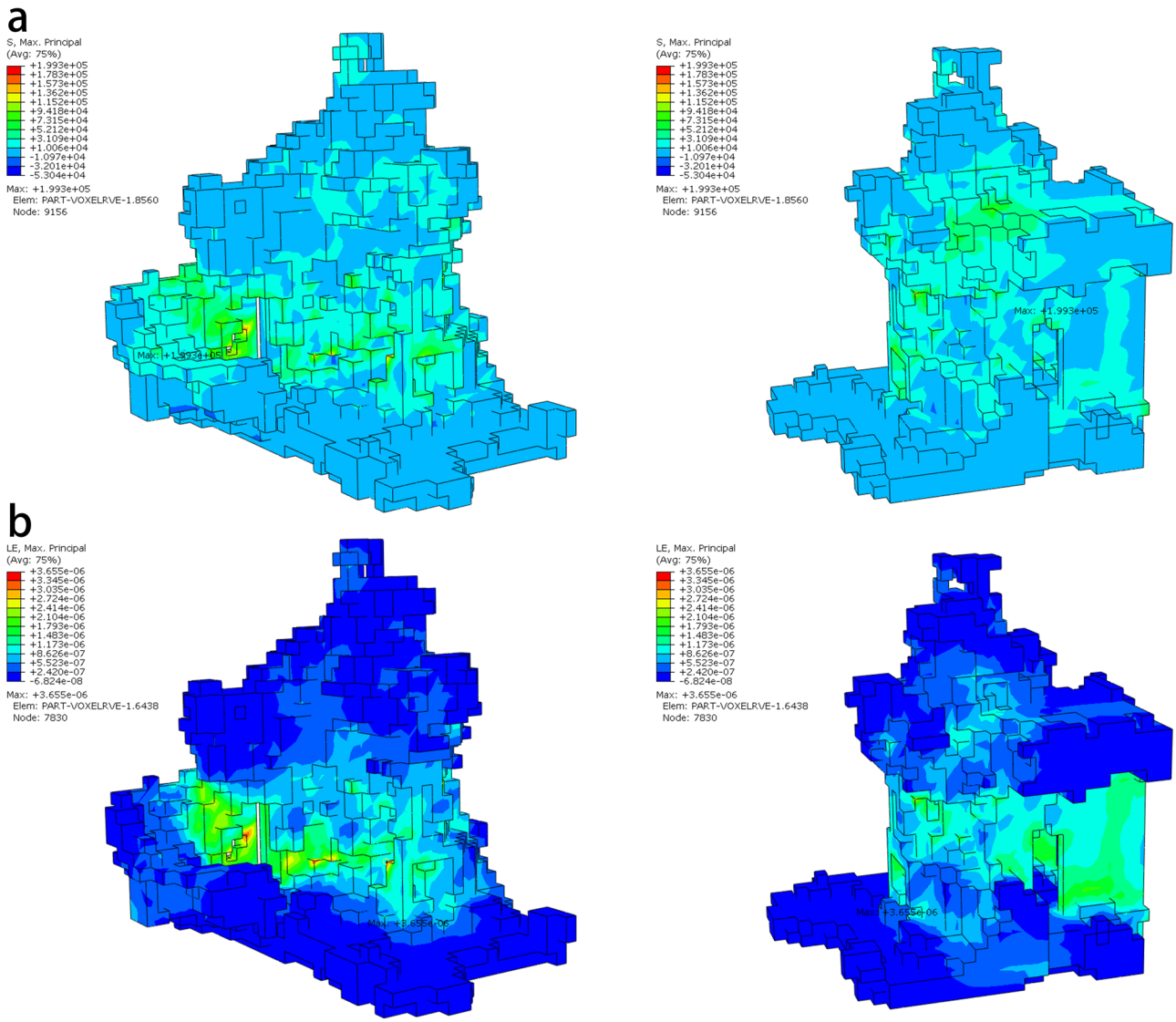

Fig. 6 | Numerical simulation results of the west zone under self-weight load. a Principal stress diagram of the west zone under self-weight load. **b** Principal strain diagram of the west zone under self-weight load.

The static analysis revealed that under the condition of full constraint of the foundation, the structure of the central cavern is relatively stable, with the maximum principal stress and maximum principal strain located at the top of the west entrance of the central cavern, ~2.2 m from the foundation. The peak of principal stress is 2.55E + 05 Pa, and the peak of principal strain is 3.21E−06 Pa, which is consistent with crack number 3.5; the stress concentration area is consistent with crack numbers 3.4 and 3.13. Through historical literature and on-site damage investigations, it can be inferred that a local foundation settlement exists in this area. However, under a complete foundation constraint, the location of the most serious crack, 3.6 in this area, showed no obvious damage. Therefore, the location of local foundation settlement can be inferred by setting the local displacement in the direction of U3 (U3 = −0.12 m). After several numerical simulations, the stress concentration area was consistent with the positions 3.5, 3.6, and 3.9 of the current investigation. The peak position of the principal stress and principal strain is close to crack No. 3.6, located in the inner wall of the east exit of the central cavern, about 0.6 m away from the foundation. The peak values of the principal stress and principal strain were 4.58E + 06 Pa, and the peak value of the principal strain is 5.92E−03 Pa. Peak value of principal stress σ_{max} reaches the critical value of maximum principal stress σ_c. Therefore, the main causes of the three cracks were determined to be the local settlement of the foundation and the general settlement region.

Stress cracks primarily caused the structural cracks from the main peak east to the central area. According to the static analysis results with full constraint at the bottom, the peak position of the principal stress is consistent with the crack No. 3.12, which is located from the peak of the main peak on the west side to the lower step of the central cavern, ~3.6 m away from the foundation. The maximum peak of the principal stress is 8.42E + 04 Pa.

Based on the finite element static simulation of 14 structural cracks in the SRMA, the main causes were determined and summarized. In the western zone, stress concentration was the leading cause of the seven cracks observed in the field investigation. From the main peak east to the central area, the stress concentration mainly caused one structural crack. Among the five structural cracks in the central cavern, crack Nos. 3.4, 3.5, and 3.13 were the main causes of stress concentration, while crack Nos 3.5, 3.6, and 3.9 were the main causes of local foundation settlement. In addition, there was another crack in the western area near the courtyard wall due to plant root cleavage by on-site damage investigation.

Cracking prediction results: A complete rockery in the central cavern was generated from the point cloud data obtained in 2021, and the cracking mode of the complete rockery model under local settlement was obtained using LEFM numerical simulation. The cracking stages of the rockery were divided according to the STATUSXFEM in Abaqus visualization results,

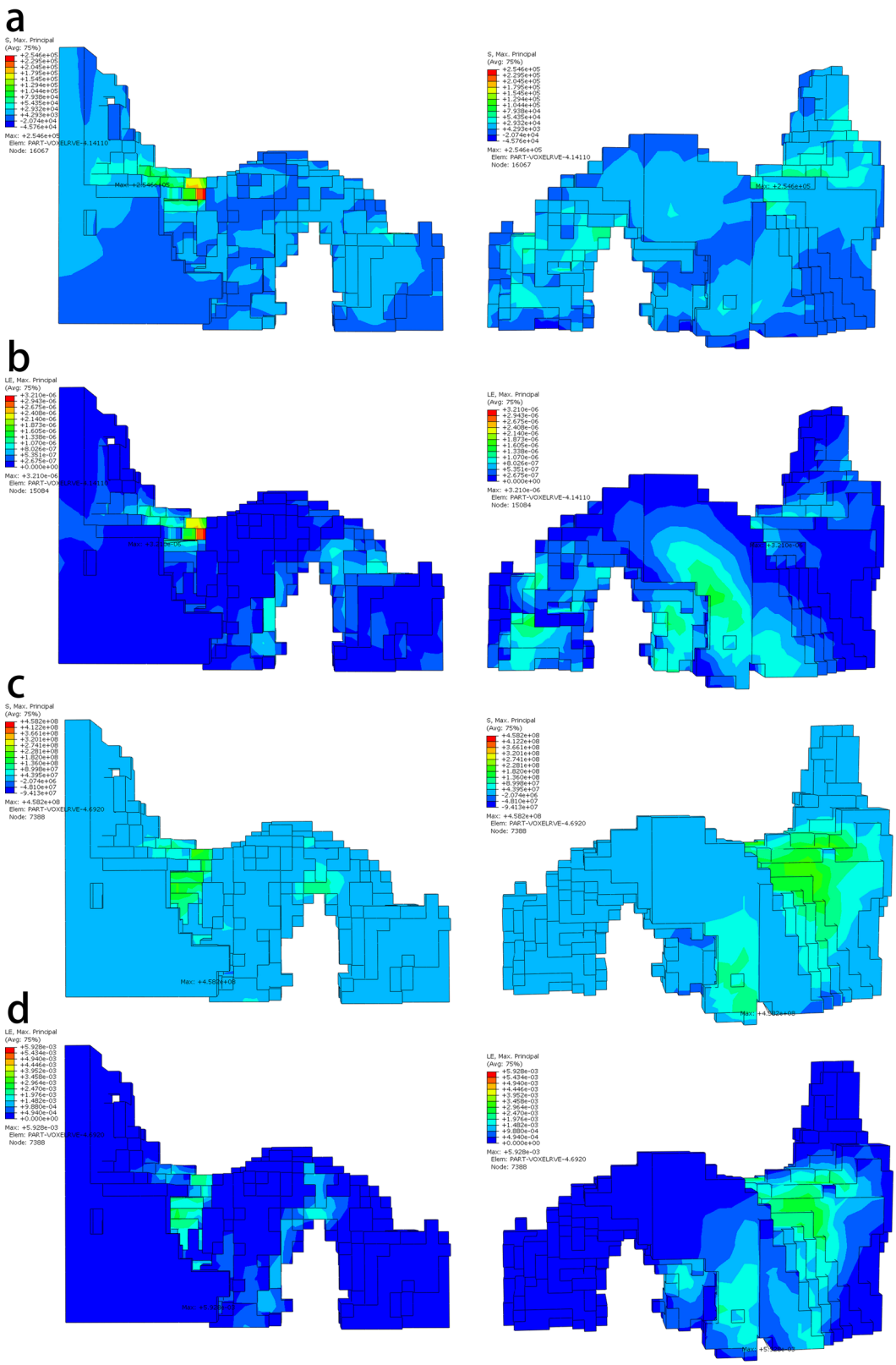

Fig. 7 | Numerical simulation of central cavern under self-weight load and local settlement of foundation. a and **b** Principal stress and principal strain diagrams of the central cavern under self-weight load. **c** and **d** Principal stress and principal strain diagrams of the central cavern under local settlement of the foundation.

combined with the crack size changes. When 0 < STATUSXFEM < 1, the rock is in the crack initiation stage. At this time, the maximum principal stress reaches the value of the crack initiation stress. When STATUSXFEM = 1, the crack passes through the first element. A change in the crack growth rate can be observed through the linear relationship between the steps and the crack size. In this process, cracks developed to a certain extent, the area no longer changed (1.844 m^2), and the volume and displacement increased sharply until the collapse of the rock. According to the observation of the cracking mode of the central cavern under the condition of local settlement, the crack initiated vertically upward from the corner of

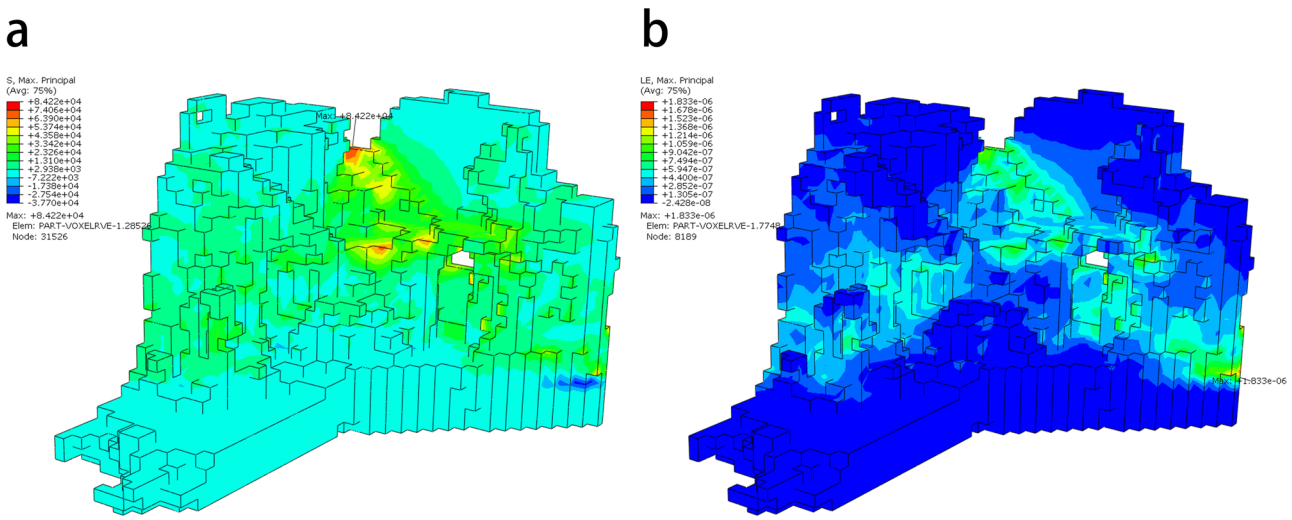

Fig. 8 | Numerical simulation of the main peak east to central area under self-weight load. a Principal stress diagram of the main peak east to the central area under self-weight load and **b** principal strain diagram.

Table 4 | Peak value and location of the principal stress and principal strain for each area of the SRMA rockery

Western zone		
Self-weight load	**Principal stress**	**Principal strain**
Peak value	199,000 Pa	0.00000366 Pa
Peak position	The middle of the entrance pillar of the west-side cavern, about 1.5 m from the foundation	The west side of the main peak, west central, about 1.25 m from the foundation
Central cavern		
Self-weight load	**Principal stress**	**Principal strain**
Peak value	254,600 Pa	0.00000321Pa
Peak position	Top of the west entrance of the central cavern, about 2.2 m from the foundation	Top of the west entrance to the central cavern, about 2.2 m from the foundation
Local settlement of foundation	**Principal stress**	**Principal strain**
Peak value	4,580,000 Pa	0.00592 Pa
Peak position	The inner wall of the east exit of the central cavern, about 0.6 m away from the foundation	The inner wall of the east exit of the central cavern, about 0.6 m away from the foundation
Main peak east to the central area		
Self-weight load	**Principal stress**	**Principal strain**
Peak value	84,200 Pa	0.00000183266 Pa
Peak position	From the peak of the main peak on the west side to the lower step of the central cavern, about 3.6 m away from the foundation	The entrance wall of the central cavern, about 0.2 m away from the foundation

the central cavern 1.2 m from the ground, slowly expanded to the entrance roof of the west side of the central cavern, and then entered the rapid expansion stage. The crack ran through the roof of the rockery and downward along the corner of the cave until it ran through the rock. Subsequently, the crack volume continued to increase rapidly until the crack growth was completed in Abaqus. The crack initiation position and expansion path of the central cavern were consistent with crack number 3.6. It was preliminarily determined that crack 3.6 was in the stage of slow crack expansion, and the crack size was also the largest. Therefore, the cracks were used for further numerical simulations of the crack expansion path.

Risk threshold and levels: In this study, the classification of crack risk level is mainly based on the SIF of Mode I crack, which is determined by solving the ratio R of Mode I crack fracture toughness K_I to its inherent fracture toughness K_{IC}. To verify the rationality of the risk level classification, a linear relationship between steps and crack size change was used to verify the mutual verification. The risk levels of each stage of crack No. 3.6 and the corresponding risk thresholds were obtained by calculation. The current area of crack No. 3.6 is 0.533 m^2. At Risk **Level I**, crack areas range from 0 to 1.571 m^2, with a critical crack area of 1.571 m^2, and a corresponding critical vertical displacement of −0.55 mm. When both the critical crack area and the critical vertical displacement are reached, the risk level escalates from **Level I (Low Risk)** to **Level II (Moderate Risk)**. Therefore, the current crack No. 3.6 remains within **Level I**. When the crack size reaches 2.136 m^2 and the vertical displacement is −1.27 mm, the crack will enter **Level III (High Risk)**. When the crack size reached 2.256 m^2, the crack area did not expand further, and the volume continued to expand until the rockery collapsed completely. However, because the rock material discussed is brittle limestone, it is necessary to focus on the changes in the initial stage of crack development, stages Level I to Level II, because the crack will expand rapidly after reaching Level III.

Table 5 | Static analysis and current crack trend for each area of the SRMA rockery

Crack number	Principal stress	Principal strain	Current crack trend
West side cavern			
3.1	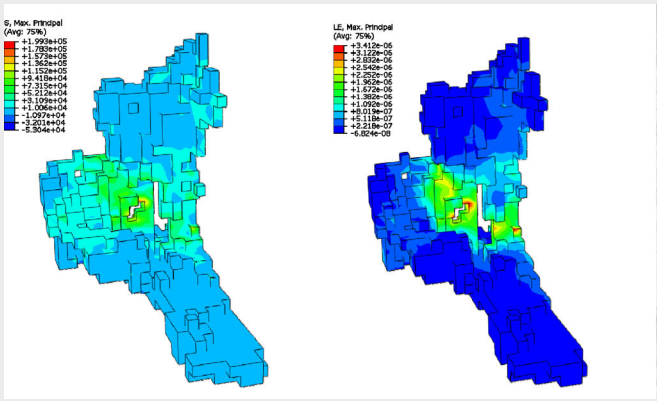		
3.2, 3.3	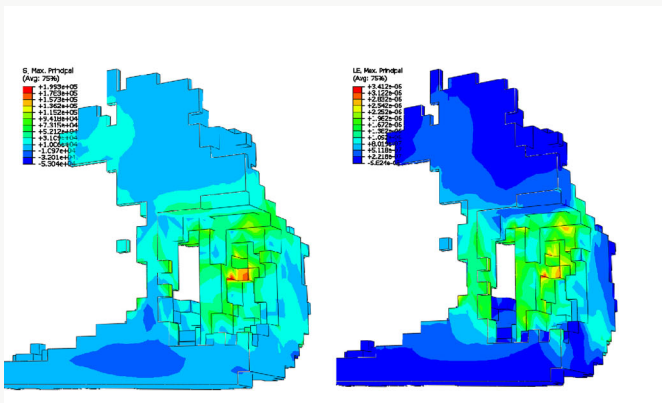		
West main peak			
3.7, 3.10	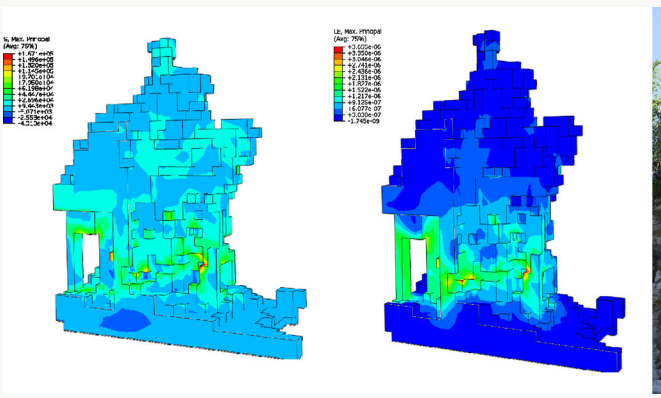		

Table 5 (continued) | Static analysis and current crack trend for each area of the SRMA rockery

Crack number	Principal stress	Principal strain	Current crack trend
3.11, 3.14	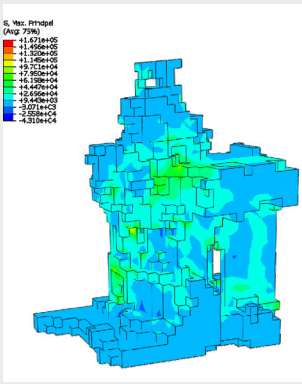	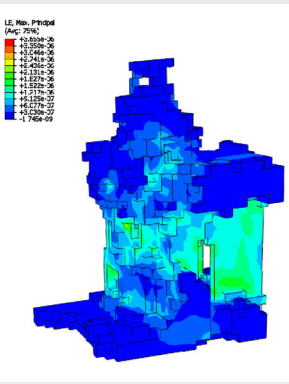	
Central cavern			
3.4, 3.13	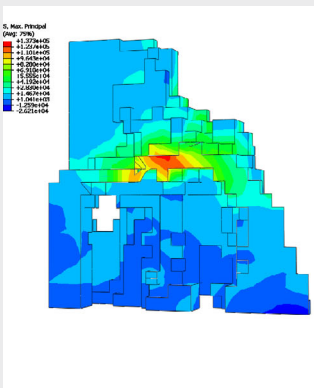	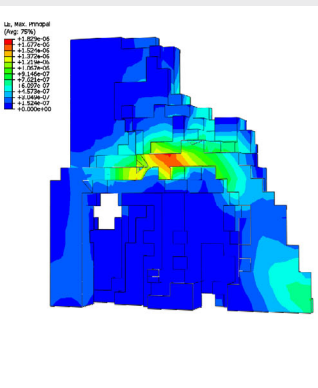	
3.5	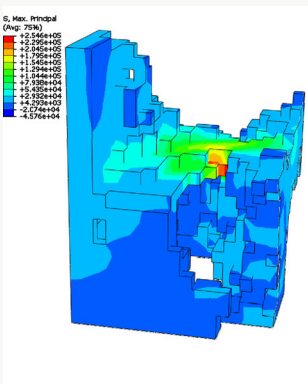	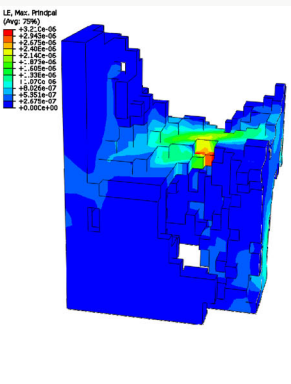	

Table 5 (continued) | Static analysis and current crack trend for each area of the SRMA rockery

Crack number	Principal stress	Principal strain	Current crack trend
3.6	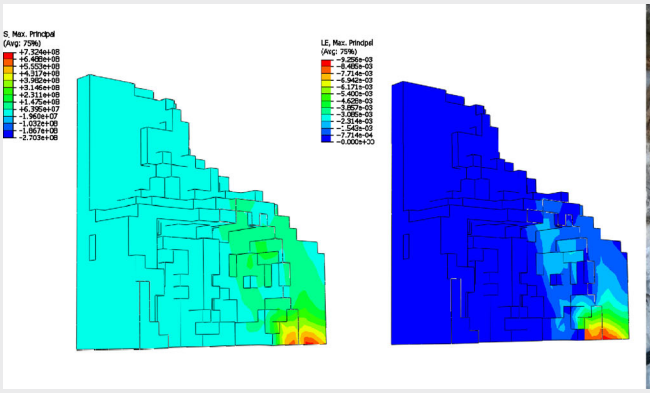		
3.9	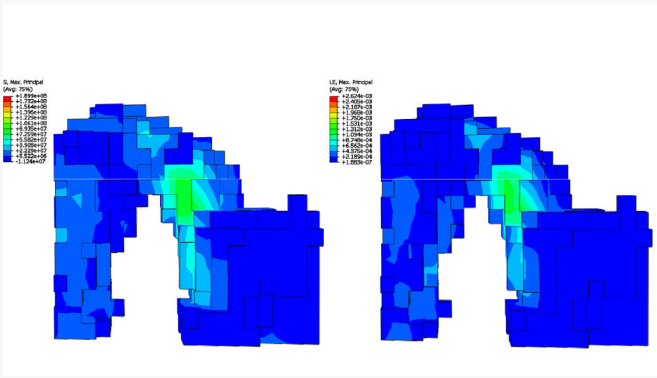		
Main peak east to central area			
3.12	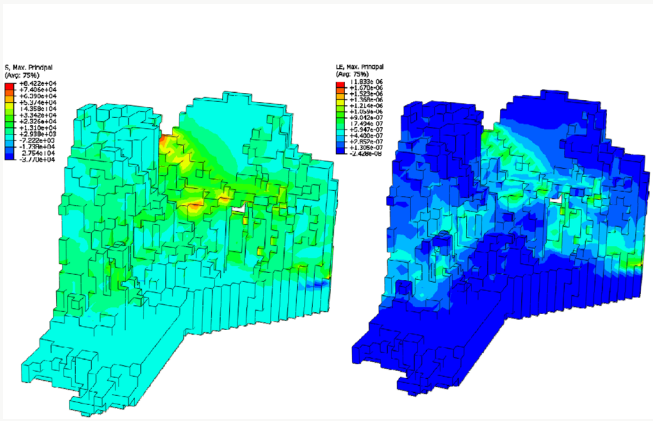		

At **Level I (Low Risk)**, the linear relationship between the steps and crack size showed that the crack growth was relatively slow, and the vertical displacement did not change significantly.

In **Level II (Moderate Risk)**, the change in crack growth increased, and the change in the vertical displacement remained weak.

At **Level III (High Risk)**, the crack area did not change after reaching 2.256 m^2, indicating that the crack had penetrated the rockery. At this time, the vertical displacement changed significantly, from −1.27 to −122.45 mm, and the crack volume increased sharply, from 0.0007 to 0.0708 m^3, until the crack development ended.

Dynamic preventive protection monitoring: Crack development in the central cavern is at a low risk. Therefore, future monitoring should focus on the local settlement of the rockery in the SRMA and changes in crack size. The results of the vertical displacement changes at special points in the central cavern obtained by numerical simulation and the change in crack growth size can be mutually verified to guide protection measures at different stages. For effective preventive protection, attention should be given to the transition from **Level I** to **Level II**, particularly the dynamic monitoring of the change in crack size. Because the change in vertical displacement is minimal, combining high-precision settlement monitoring technology is necessary. There are currently some limitations for dynamic monitoring. This study proposes a research method for determining the crack propagation risk threshold of classical garden rockeries. Point cloud data collected from the SRMA rockery in 2021 were used to generate the initial calculation results. A second round of data collection was conducted in February 2025 to preliminarily validate these results. However, no dynamic monitoring was performed during the intervening period, resulting in a lack of coherent point cloud data for this rockery. Therefore, following the establishment of quantitative risk levels and thresholds, future studies should incorporate regular dynamic monitoring to track temporal changes in relevant parameters. In addition to the incomplete collection of historical point cloud data, another limitation is that structural crack monitoring in this study primarily relied on on-site damage investigation and 3D model reconstruction based on point cloud data. In future work, information technologies for identifying crack features within 3D models[45], combined with historical point cloud comparison techniques, could enable dynamic monitoring of crack size changes at a finer scale.

Table 6 | The leading causes of structural cracks of the SRMA rockery

Crack number	Length (cm)	Width (mm)	Depth (mm)	Leading causes
3.1	92	10.48	90.58	D
3.2	50	4.24	57.81	D
3.3	51	2.41	18.88	D
3.4	10.5	3.65	14.89	D
3.5	61	/	31.51	AD
3.6	100	3.94	54.79	A
3.7	35	4.76	31.16	D
3.8	/	/	/	E
3.9	60	/	/	A
3.10	39	2.2	27.57	D
3.11	80	2.2	0.94	D
3.12	48	/	/	D
3.13	7	2.74	4.58	D
3.14	/	/	/	D

Compared with existing risk assessment methods for rockeries, no literature to date has adopted a similar approach to evaluate the crack propagation risk in classical garden rockeries. Therefore, this study is methodologically innovative. This study introduces LEFM, which is suitable for analyzing the fracture behavior of typical brittle materials, to the risk assessment of classical garden rockery structures. A voxel-based finite element modeling approach is employed, which yields comparable results to other equivalent finite element methods but offers superior computational efficiency[46,47]. Furthermore, the application of XFEM to numerically simulate structural damage in cultural heritage rockeries addresses a critical gap in the risk analysis of crack propagation in such structures. Therefore, compared with existing approaches, this study integrates rock fracture mechanics theory and the extended finite element method into the risk assessment of cultural heritage rockeries. It provides a practical and engineering-oriented method that simplifies finite element modeling and improves operational efficiency. Future research may further explore ways to better balance prediction accuracy and computational performance. To further illustrate its practical value, the specific advantages of this method are summarized as follows.

The leading causes of structural cracks in the rockery were identified through mechanical analysis. During the damage investigation stage, the location, length, width, depth, and probable causes of each crack can be determined based on historical literature and on-site inspection. Through the static analysis process of preliminary damage diagnosis, non-structural cracks can be effectively excluded, incorrect causal attributions can be corrected, potential crack initiation points can be identified, and objective damage diagnosis reports for each structural crack can be produced. These methods are effective for identifying key monitoring areas and guiding preventive protection strategies. For instance, if structural cracks are caused by local foundation settlement, it is essential to regularly monitor foundation displacement trends and associated crack size variations. If structural cracks result from tourist loads, it becomes necessary to manage the number and frequency of tourists climbing on the rockeries.

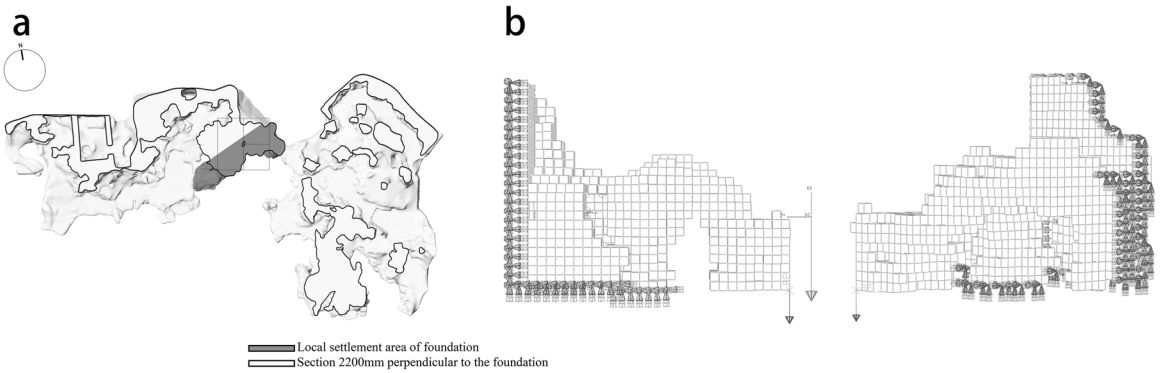

Fig. 9 | The area of local settlement in the rockery foundation and the corresponding interaction relationship settings in Abaqus. a Foundation settlement area plan and **b** Interaction relationship.

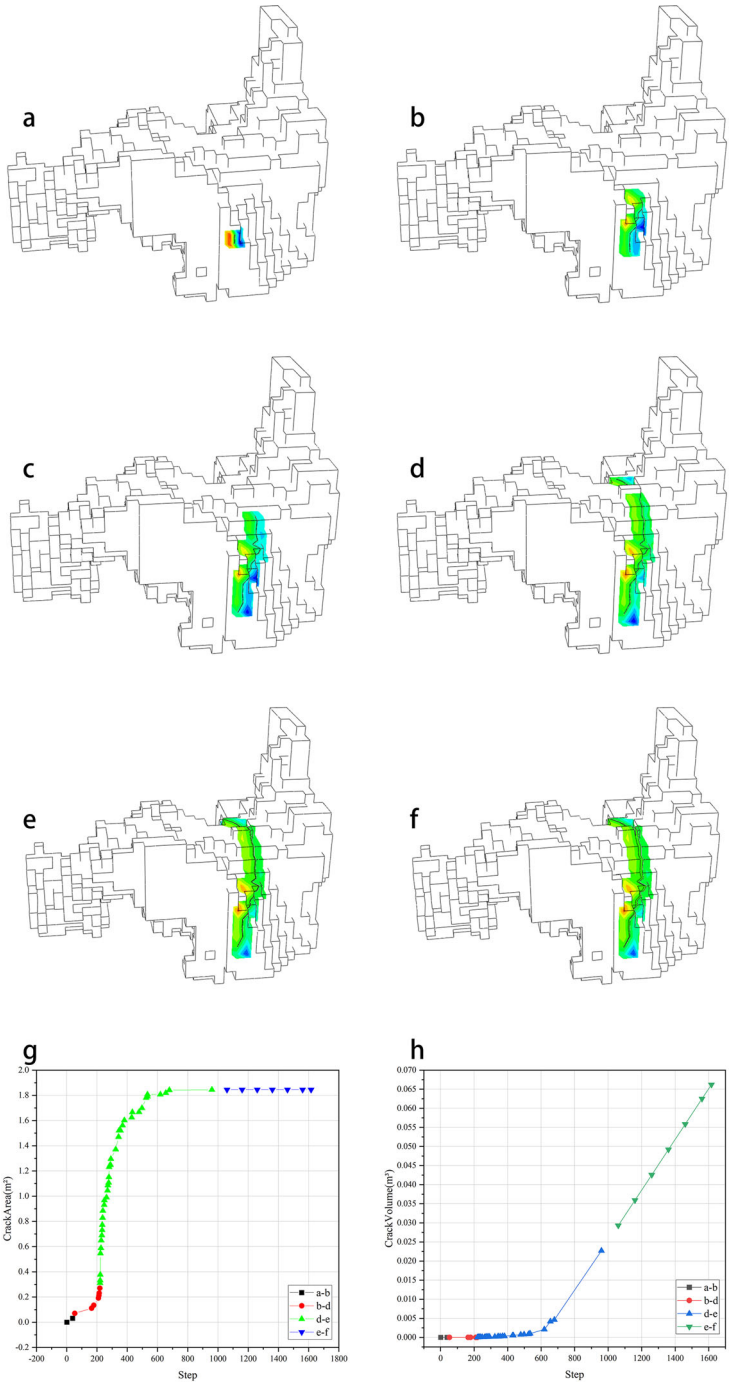

Fig. 10 | Prediction of rockery cracking mode. **a** Initiation position, (**b**) Cracks through the first element. **b–d** Crack develops slowly. **d–f** Crack develops rapidly. **e** Cracks through the rockery. **f** Cracking ends. **g** Linear relationship between steps and crack area. **h** Linear relationship between steps and crack volume.

The rockery's crack mode and crack growth path were predicted using LEFM. The cracking mode of the rockery, as determined through LEFM numerical simulation, can be cross-validated with the crack damage diagnosis report to further identify the primary cause of each crack. For instance, under conditions of local foundation settlement, the crack pattern observed in the central cavern corresponds to crack No. 3.6. This supports the conclusion that local settlement is the primary cause of cracking in this area. Based on this finding, the risk threshold for crack No. 3.6 was calculated to provide an objective basis for evaluating its structural risk.

The risk threshold, risk level, and preventive protection strategy against rock cracks were determined effectively. In this study, He Garden was used as a case study to implement the full workflow of damage investigation and data processing, leading to the generation of a structural crack diagnosis report for the rockery. The extended finite element method was applied to simulate the rockery's crack propagation mode and predict the crack growth path. As a result, the crack risk levels and risk thresholds at each stage were determined, demonstrating the feasibility of this numerical simulation system for assessing crack development risk in cultural heritage rockeries. This system offers an objective reference for guiding the preventive protection of rockeries with significant structural cracking.

To develop a comprehensive crack propagation risk assessment system, future studies should consider incorporating a broader set of influencing factors. The classification of crack risk level was primarily based on the ratio (R) of the Mode I SIF K_I to the material's inherent fracture toughness K_{IC}. This study conducts numerical simulations on rockeries exhibiting prominent structural risk cracks. In future research, a plastic constitutive model may be introduced to evaluate rockeries with broader potential risks. For instance, studying the plastic zones of rockeries can help simulate

Table 7 | Different stages of rockery cracking modes

Stage	Step	Frame time (s)	Area (m^2)	Volume (m^3)	S Max principal (Pa)	Displacement (P4) (mm)
a	9	0.0003	0	0	2.09E + 06	−0.0398
b	39	0.0019	0.031	0.000001	6.54E + 06	−0.2263
c	53	0.0021	0.071	0.000002	4.86E + 06	−0.2504
d	210	0.004	0.192	0.000012	1.08E + 07	−0.4756
e	960	0.3446	1.844	0.022692	1.21E + 09	−41.3502
f	1616	1	1.844	0.066202	3.54E + 09	−120

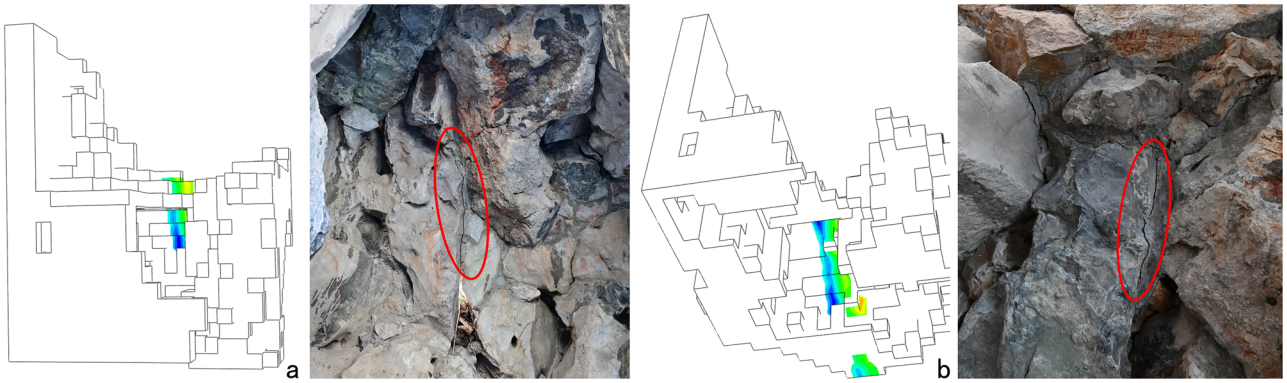

Fig. 11 | Comparison diagram of crack model prediction and current situation. a Crack prediction corresponding to crack number 3.6 and **b** Cracking prediction corresponding to crack number 3.5.

Table 8 | 3.6 Classification of crack risk level

Risk level	Frame time (s)	*R*	Displacement (mm)	Crack volume (m^3)	Crack area (m^2)
I	0.00001	0.002	−0.0012	0	0.533
	0.00002	0.004	−0.0024	0	0.533
	0.00004	0.007	−0.0042	0	0.533
	0.00006	0.011	−0.0069	0	0.533
	0.00009	0.018	−0.01095	0	0.533
	0.00014	0.028	−0.017025	0.000001	0.533
	0.00022	0.043	−0.026138	0.000001	0.533
	0.00033	0.066	−0.039806	0.000002	0.533
	0.0005	0.099	−0.060309	0.000003	0.533
	0.00076	0.15	−0.08925	0.000004	0.533
	0.00114	0.226	−0.131955	0.000006	0.533
	0.00172	0.34	−0.203153	0.000011	0.533
	0.00259	0.511	−0.30476	0.000026	0.573
	0.00359	0.709	−0.425541	0.000055	0.808
	0.00459	**0.907**	**−0.551409**	**0.000157**	**1.571**
II	0.00559	1.105	−0.675731	0.000194	1.571
	0.00659	1.303	−0.785845	0.00033	1.848
	0.00759	1.501	−0.905718	0.000418	2.021
	0.00859	1.698	−1.02196	0.000487	2.092
	0.00959	1.896	−1.15148	0.000565	2.131
	0.01058	**2.094**	**−1.27081**	**0.00068**	**2.136**
III	0.0109	2.292	−1.32986	0.000773	2.222
	0.0175	3.479	−2.13681	0.001244	2.241
	0.0198	**3.874**	**−2.41901**	**0.001394**	**2.256**
	0.02	4.072	−2.45221	0.001413	2.256

Table 8 (continued) | 3.6 Classification of crack risk level

Risk level	Frame time (s)	*R*	Displacement (mm)	Crack volume (m^3)	Crack area (m^2)
	0.0305	6.051	−3.72795	0.002146	2.256
	0.0405	8.029	−4.95214	0.002852	2.256
	0.0505	10.007	−6.17632	0.003557	2.256
	0.0605	11.985	−7.40051	0.004262	2.256
	0.0705	13.964	−8.6247	0.004968	2.256
	0.0805	15.942	−9.84889	0.005673	2.256
	0.0905	17.921	−11.0731	0.006379	2.256
	0.1	19.701	−12.2973	0.007085	2.256
	0.2	39.484	−24.8	0.014117	2.256
	0.3	59.267	−36.7995	0.021173	2.256
	0.4	79.047	−49.044	0.028242	2.256
	0.5	98.833	−61.2887	0.035321	2.256
	0.6	118.613	−73.5334	0.042412	2.256
	0.7	138.4	−85.7781	0.049514	2.256
	0.8	158.18	−98.0228	0.056627	2.256
	0.9	177.967	−110.267	0.063752	2.256
	1	**197.827**	**−122.445**	**0.070849**	**2.256**

The bold values identifies rows corresponding to the transition from risk level I to II, from II to III, the calculation end point, and the point where the crack area remains unchanged.

structural instability in the overall rockery. In addition to load-induced stress, factors such as high temperature[48] and water infiltration[49] may also contribute to structural degradation. These elements may induce coupled damage mechanisms[50], therefore, numerical modeling incorporating multi-field coupling can be developed to further assess the crack propagation risks in cultural heritage rockeries. While this study focuses solely on crack propagation risk in terms of structural stability, it does not address the

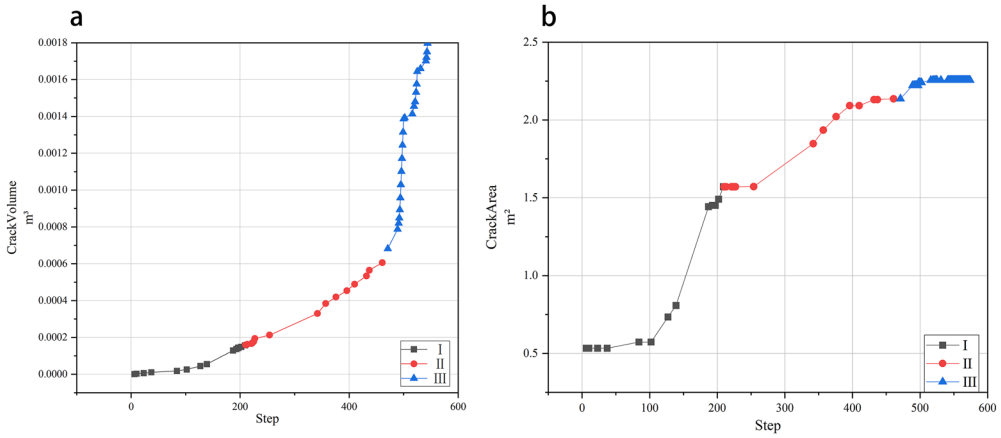

Fig. 12 | Crack size change. a Line diagram of the relationship between analysis steps and crack volume and **b** line diagram of the relationship between analysis steps and crack area.

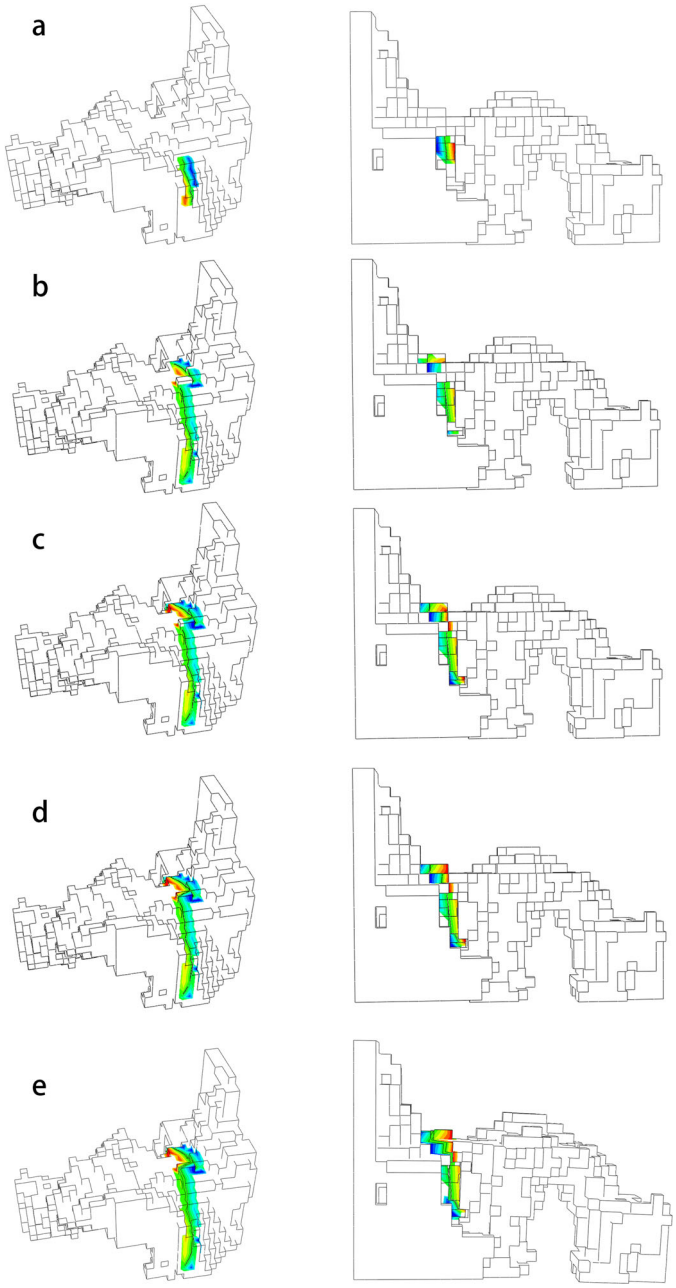

Fig. 13 | Visualization of each stage of crack development. a Initial crack state, **b** critical state marking the transition from Risk Level I to Risk Level II ($R = 1$), **c** critical state marking the transition from Risk Level II to Risk Level III ($R = 2$), **d** formation of through-cracks, and **e** expansion over.

Table 9 | Crack 3.6 risk threshold

Risk level	Frame time (s)	*R*	Crack area (m^2)	Crack volume (m^3)	Displacement (mm)
I	(0,0.005)	(0,1)	(0,1.571)	(0,0.0002)	(0,−0.55)
II	[0.005,0.011)	[1,2)	[1.571,2.136)	[0.0002,0.0007)	[−0.55,−1.27)
III	[0.011,1]	[2,198]	[2.136,2.256]	[0.0007,0.0708]	[−1.27,−122.45]

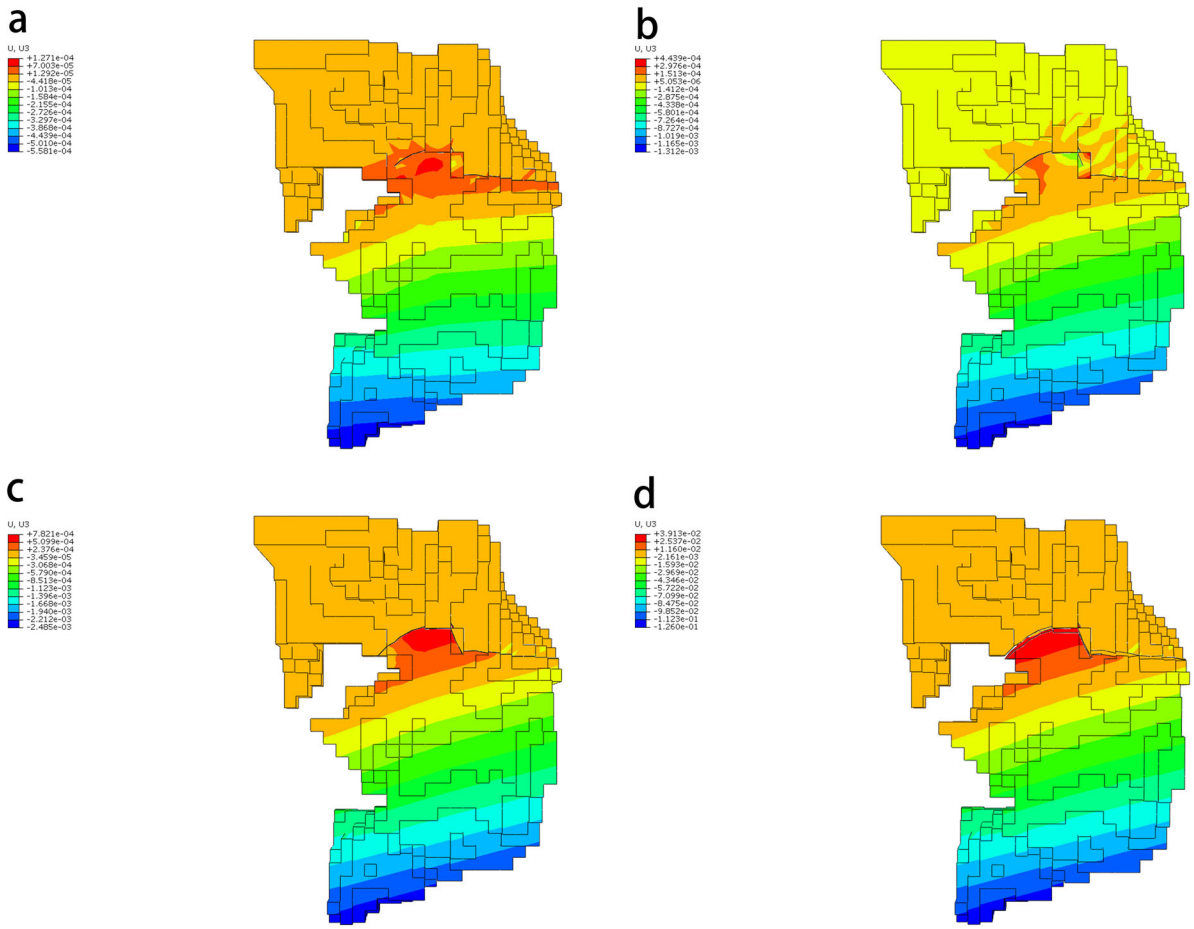

Fig. 14 | Overall displacements from low risk to high risk. a Diagram of critical displacements from I to II, **b** diagram of critical displacements from II to III, **c** crack through the rockery displacement diagram, and **d** extension end displacement diagram.

Table 10 | Vertical displacement changes of special points

Risk level	Frame time (s)	*P*1 (mm)	*P*2 (mm)	*P*3 (mm)	*P*4 (mm)	*P*5 (mm)	*P*6 (mm)	Max displacement (mm)
I	0.00001	−0.000036	−0.000236	−0.000753	−0.001119	−0.001200	−0.000743	−0.001200
	0.00002	−0.000071	−0.000471	−0.001505	−0.002238	−0.002400	−0.001485	−0.002400
	0.00004	−0.000125	−0.000825	−0.002634	−0.003916	−0.004200	−0.002599	−0.004200
	0.00006	−0.000206	−0.001355	−0.004327	−0.006433	−0.006900	−0.004270	−0.006900
	0.00009	−0.000326	−0.002151	−0.006867	−0.010209	−0.010950	−0.006776	−0.010950
	0.00014	−0.000507	−0.003344	−0.010676	−0.015873	−0.017025	−0.010536	−0.017025
	0.00022	−0.000779	−0.005134	−0.016391	−0.024369	−0.026138	−0.016175	−0.026138
	0.00033	−0.001186	−0.007819	−0.024962	−0.037113	−0.039806	−0.024634	−0.039806
	0.0005	−0.001760	−0.011845	−0.037811	−0.056260	−0.060309	−0.037254	−0.060309
	0.00076	−0.002247	−0.017430	−0.055853	−0.083465	−0.089250	−0.054615	−0.089250
	0.00114	−0.003225	−0.025779	−0.082558	−0.123501	−0.131955	−0.080539	−0.131955
	0.00172	−0.003700	−0.039559	−0.126783	−0.191136	−0.203153	−0.121743	−0.203153
	0.00259	−0.003660	−0.059734	−0.189823	−0.288911	−0.304760	−0.178158	−0.304760
	0.00359	−0.001288	−0.082475	−0.263989	−0.405785	−0.425541	−0.242996	−0.425541
	0.00459	**0.00923955**	**−0.105741**	**−0.339317**	**−0.534393**	**−0.551409**	**−0.29549**	**−0.551409**
II	0.00559	0.012486	−0.129059	−0.415453	−0.655319	−0.675731	−0.360811	−0.675731
	0.00659	0.016452	−0.163789	−0.485193	−0.780053	−0.785845	−0.389642	−0.785845

Table 10 (continued) | Vertical displacement changes of special points

Risk level	Frame time (s)	*P*1 (mm)	*P*2 (mm)	*P*3 (mm)	*P*4 (mm)	*P*5 (mm)	*P*6 (mm)	Max displacement (mm)
	0.00759	0.019987	−0.191316	−0.559427	−0.902981	−0.905718	−0.442198	−0.905718
	0.00859	0.025238	−0.214439	−0.630337	−1.019620	−1.021960	−0.496379	−1.021960
	0.00959	0.028177	−0.243949	−0.710707	−1.151370	−1.151480	−0.555343	−1.151480
	0.01058	**0.031574**	**−0.272926**	**−0.781162**	**−1.27081**	**−1.26438**	**−0.598882**	**−1.27081**
III	0.0109	0.034756	−0.295738	−0.808026	−1.329860	−1.304520	−0.586582	−1.329860
	0.0175	0.055896	−0.475152	−1.298290	−2.136810	−2.096080	−0.942436	−2.136810
	0.0198	**0.064007**	**−0.538514**	**−1.468570**	**−2.419010**	**−2.370980**	**−1.062490**	**−2.419010**
	0.02	0.064888	−0.545902	−1.488720	−2.452210	−2.403510	−1.0770660	−2.452210
	0.0305	0.099491	−0.828977	−2.263080	−3.727950	−3.654330	−1.637790	−3.727950
	0.0405	0.132326	−1.101030	−3.006140	−4.952140	−4.854330	−2.175490	−4.952140
	0.0505	0.165242	−1.373000	−3.749170	−6.176320	−6.054330	−2.713120	−6.176320
	0.0605	0.198239	−1.644890	−4.492150	−7.400510	−7.254330	−3.250700	−7.400510
	0.0705	0.231318	−1.916700	−5.235100	−8.624700	−8.454330	−3.788220	−8.624700
	0.0805	0.264478	−2.188420	−5.978000	−9.848890	−9.654330	−4.325690	−9.848890
	0.0905	0.297720	−2.460070	−6.720860	−11.073100	−10.854300	−4.863090	−11.073100
	0.1	0.331043	−2.73163	−7.46369	−12.2973	−12.0543	−5.40044	−12.2973
	0.2	0.675518	−5.503320	−15.046000	−24.800000	−24.305700	−10.876400	−24.800000
	0.3	1.014350	−8.153970	−22.319900	−36.799500	−36.065700	−16.130200	−36.799500
	0.4	1.368140	−10.850500	−29.738200	−49.044000	−48.065700	−21.485600	−49.044000
	0.5	1.730070	−13.538800	−37.152400	−61.288700	−60.065700	−26.835200	-61.288700
	0.6	2.100130	−16.218800	−44.562600	−73.533400	−72.065700	−32.179300	−73.533400
	0.7	2.478300	−18.890300	−51.968700	−85.778100	−84.065700	−37.517800	−85.778100
	0.8	2.864600	−21.553500	−59.370800	−98.022800	−96.065700	−42.850800	−98.022800
	0.9	3.259010	−24.208200	−66.768700	−110.267000	−108.066000	−48.178500	−110.267000
	1	**3.659320**	**−26.839800**	**−74.122100**	**−122.445000**	**−120.000000**	**−53.471900**	**−122.445000**

The bold values identifies rows corresponding to the transition from risk level I to II, from II to III, the calculation end point, and the point where the crack area remains unchanged.

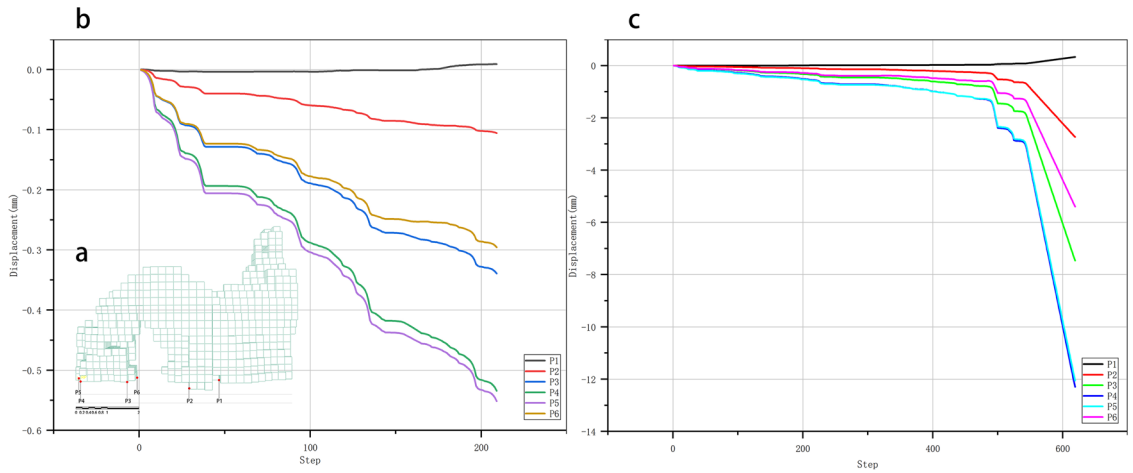

Fig. 15 | Special point displacement changes from low risk to high risk. a Special point position, **b** I–II special point displacement changes, and **c** I–III special point displacement changes.

Fig. 16 | 3D scanning position. The red square area represents the region where the two scans conducted in 2021 and 2025 are compared.

impact of crack development on aesthetic qualities. Future research could examine the relationship between crack spatial distribution and garden visual corridors using visual domain analysis tools.

The experimental results indicate that the transition from Risk Level I to Risk Level II in crack propagation warrants particular attention. The fracture toughness of brittle rock materials increases sharply as cracking progresses and exhibits significant variation with displacement, crack size, and related parameters. The low and moderate risk stages constitute only a small portion of the entire crack development process. During this phase, displacement changes are minimal, while the crack area expands slowly at first and then continuously, eventually stabilizing. Once the crack enters the high-risk stage,

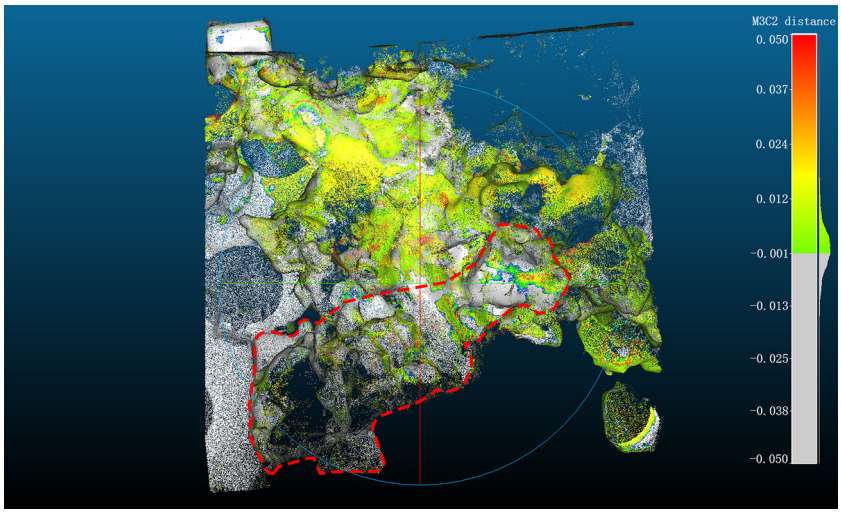

Fig. 17 | Comparative deformation maps of the central cavern in 2021 and 2025. The area represented by the red dotted line is the region with significantly negative values after comparing the two scans conducted in 2021 and 2025.

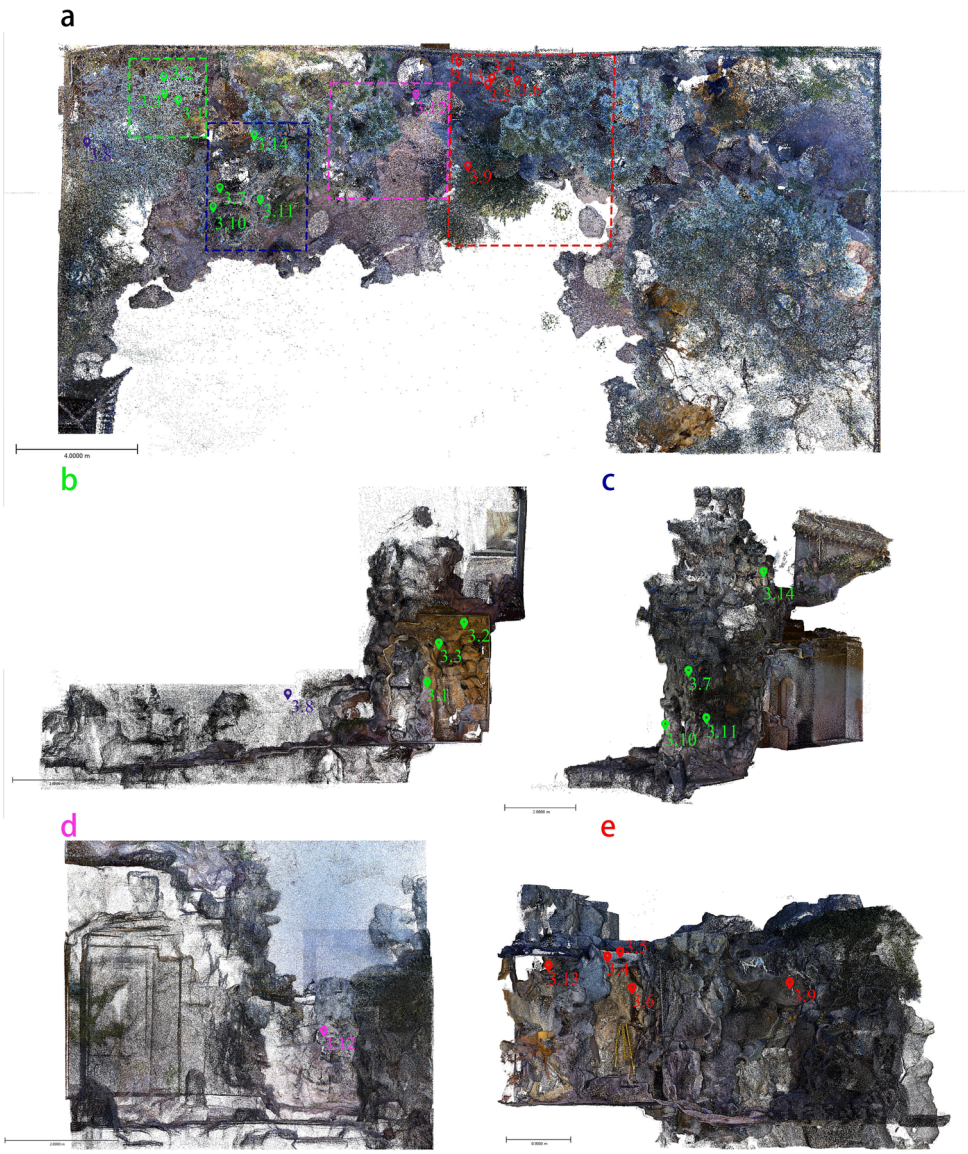

Fig. 18 | Structural crack location marking. a Plane location marking of structural crack of SRMA. **b** Location of cracks in the west side cavern. **c** Location of cracks in the west main peak. **d** Location of cracks from the main peak east to central area. **e** Location of cracks in central cavern.

it gradually penetrates the rockery, with a sharp increase in displacement and a rapid rise in crack volume. This behavior aligns with the crack propagation characteristics of brittle rocks under linear elastic fracture mechanics and the damage evolution laws of limestone. Therefore, for effective dynamic monitoring and preventive protection of crack propagation in rockeries, close attention should be paid to variations in key deterioration indicators during both the initial and stable propagation stages to prevent the formation of through-cracks. This approach holds practical engineering significance for rock monitoring and the preservation of cultural heritage.

Data availability

The data sets used in this study are available from the corresponding author upon request.

Received: 23 April 2025; Accepted: 21 September 2025;
Published online: 23 October 2025

References

1. Fu, L. et al. A multi-criteria decision-making approach to assessing the health risk of rockeries in Chinese classical gardens. *Herit. Sci.* **11**, 92 (2023).
2. Liang, H. et al. How to survey, model, and measure rockeries in a Chinese classical garden: a case study for Huanxiu Shanzhuang, Suzhou, *China*. *Landsc. Res.* **45**, 377–391 (2020).
3. Lou, L. et al. Cave feature extraction and classification from rockery point clouds acquired with handheld laser scanners. *Herit. Sci.* **10**, 177 (2022).
4. Dong, Q., Zhang, Q. & Zhu, L. 3D scanning, modeling, and printing of Chinese classical garden rockeries: Zhanyuan's South Rockery. *Herit. Sci.* **8**, 1–15 (2020).
5. Wang, Z. et al. Digital improvements in the design and construction process of classical Chinese garden rockeries: a study based on material digitization. *Herit. Sci.* **12**, 327 (2024).
6. Wang, Y. et al. Volume calculation methods of irregular stone artifacts based on 3D laser scanning technology. *J. Asian Arch. Build. Eng.* **22**, 3386–3402 (2023).
7. Korumaz, M. et al. An integrated Terrestrial Laser Scanner (TLS), Deviation Analysis (DA), and Finite Element (FE) approach for health assessment of historical structures. A minaret case study. *Eng. Struct.* **153**, 224–238 (2017).
8. Hu, B. et al. Crack cause in the high slope of Chinese ancient copper mine relics: a three-dimensional non-linear finite difference analysis. *IEEE Access* **8**, 13987–13997 (2020).
9. Khaloo, A., Khoshnevis, A. & Yekrangnia, M. On the vulnerability of the Shrine of Prophet Daniel through field observation and numerical simulation. *Eng. Fail. Anal.* **102**, 237–259 (2019).
10. Betti, M. & Vignoli, A. Numerical assessment of the static and seismic behaviour of the basilica of Santa Maria all'Impruneta (Italy). *Constr. Build. Mater.* **25**, 4308–4324 (2011).
11. Betti, M., Orlando, M. & Vignoli, A. Static behaviour of an Italian Medieval Castle: damage assessment by numerical modelling. *Comput. Struct.* **89**, 1956–1970 (2011).
12. Alessandri, C. et al. Crack patterns induced by foundation settlements: Integrated analysis on a renaissance masonry palace in Italy. *Int J. Arch. Herit.* **9**, 111–129 (2015).
13. Tralli, A. et al. Masonry structures in the presence of foundation settlements and unilateral contact problems. *Int. J. Solids Struct.* **191**, 187–201 (2020).
14. Vlcko, J. et al. Rock displacement and thermal expansion study at historic heritage sites in Slovakia. *Environ. Geol.* **58**, 1727–1740, (2009).
15. Drougkas, A. et al. In-plane seismic behaviour of retrofitted masonry walls subjected to subsidence-induced damage. *Eng. Struct.* **223**, 111192 (2020).
16. Ávila, F., Puertas, E. & Gallego, R. Probabilistic reliability assessment of existing masonry buildings: the church of San Justo y Pastor. *Eng. Struct.* **223**, 111160 (2020).
17. Blyth, A., Napolitano, R. & Glisic, B. Documentation, structural health monitoring and numerical modelling for damage assessment of the Morris Island Lighthouse. *Philos. Trans.* **377**, 20190002 (2019).
18. Wang, X. et al. The history of rescuing reinforcement and the preliminary study of preventive protection system for the cliff of Mogao Grottoes in Dunhuang, *China*. *Herit. Sci.* **9**, 1–18 (2021).
19. Dong, Q. et al. Intangible cultural heritage based on finite element analysis: force analysis of Chinese traditional garden rockery construction. *Herit. Sci.* **12**, 241 (2024).
20. Zhang, Q., Wang, C. & Zhang, X. Research on the disease monitoring and structural protection of garden rockery heritage based on an finite element analysis. *J. Nanjing Univ.* **48**, 252 (2024).
21. Fu, L., Zhi, H. & Zhang, Q. A risk index for the structural diagnosis of rockeries in Chinese classical gardens based on the MIVES model. *npj Herit. Sci.* **13**, 37 (2025).
22. Valente, M. & Milani, G. Damage assessment and partial failure mechanisms activation of historical masonry churches under seismic actions: three case studies in Mantua. *Eng. Fail Anal.* **92**, 495–519 (2018).
23. Malcata, M. et al. Failure analysis of a Portuguese cultural heritage masterpiece: Bonet building in Sintra. *Eng. Fail Anal.* **115**, 104636 (2020).
24. Ávila, F. et al. Influence of crack propagation on the seismic behavior of historic rammed earth buildings: the Tower of Muhammad in the Alhambra (Spain). *Eng. Struct.* **301**, 117365 (2024).
25. Preciado, A. et al. Damage description and schematic crack propagation in Colonial Churches and old masonry buildings by the 2017 Puebla-Morelos earthquakes (M_w = 8.2 and 7.1). *Eng. Fail Anal.* **141**, 106706. (2022).
26. Wang, S. et al. Numerical studies on micro-cracking behavior of transversely isotropic argillaceous siltstone in Longyou Grottoes under three-point bending. *Theor. Appl Fract. Mech.* **122**, 103638. (2022).
27. Diz-Mellado, E. et al. Non-destructive testing and finite element method integrated procedure for heritage diagnosis: the Seville Cathedral case study. *J. Build Eng.* **37**, 102134. (2021).
28. Zhang, Y. L. & Feng, X. T. Extended finite element simulation of crack propagation in fractured rock masses. *Mater. Res. Innov.* **15**(Suppl. 1), s594–s596 (2011).
29. Asem, P. et al. On tensile fracture of a brittle rock. *Int. J. Rock. Mech. Min. Sci.* **144**, 104823 (2021).
30. Park, I. B. & Lee, C. I. Mixed-mode crack propagation in rock using numerical analysis. *Int J. Rock. Mech. Min. Sci.* **41**, 31–36 (2004).
31. Budyn, É, ZI, G., Moës, N. & Belytschko, T. A method for multiple crack growth in brittle materials without remeshing. *Int. J. Numer. Methods Eng.* **61**, 1741–1770 (2004).
32. Moës, N., Dolbow, J. & Belytschko, T. A finite element method for crack growth without remeshing. *Int. J. Numer. Methods Eng.* **46**, 131–150 (1999).
33. Pesci, A. et al. Laser scanning and digital imaging for the investigation of an ancient building: Palazzo d'Accursio study case (Bologna, Italy). *J. Cult. Herit.* **13**, 215–220 (2012).
34. Pegon, P., Pinto, A. V. & Géradin, M. Numerical modelling of stone-block monumental structures. *Comput Struct.* **79**, 2165–2181 (2001).
35. Castellazzi, G. et al. Cloud2FEM: a finite element mesh generator based on point clouds of existing/historical structures. *SoftwareX* **18**, 101099 (2022).
36. D'Altri, A. M., De Miranda, S., Castellazzi, G. & Glisic, B. Numerical modelling-based damage diagnostics in cultural heritage structures. *J. Cult. Herit.* **61**, 1–12 (2023).
37. Pesci, A., Casula, G. & Boschi, E. Laser scanning the Garisenda and Asinelli towers in Bologna (Italy): detailed deformation patterns of two ancient leaning buildings. *J. Cult. Herit.* **12**, 117–127 (2011).

38. Khoramishad, H., Akbardoost, J. & Ayatollahi, M. Size effects on parameters of cohesive zone model in mode I fracture of limestone. *Int. J. Damage Mech.* **23**, 588–605 (2013).
39. Zhou et al. Effect of loading rate on fracture characteristics of rock. *J. Cent. South Univ. Technol.* **17**, 150–155 (2010).
40. Liu, D., Chen, H., Su, R. K. L., Chen, L. & Liang, K. Influence of initial crack length on fracture properties of limestone using DIC technique. *Constr. Build. Mater.* **403**, 133020 (2023).
41. Aliha, M. R. M., Sistaninia, M., Smith, D. J., Pavier, M. J. & Ayatollahi, M. R. Geometry effects and statistical analysis of mode I fracture in guiting limestone. *Int. J. Rock Mech. Min.* **51**, 128–135 (2012).
42. Yang, C. et al. Digital characterization of the surface texture of Chinese classical garden rockery based on point cloud visualization: small-rock mountain retreat. *Herit. Sci.* **11**, 13 (2023).
43. Bamonte, P. et al. Crack patterns in double-wall industrial masonry chimneys: Possible causes and numerical modelling. *J. Cult. Herit.* **47**, 133–142 (2021).
44. Ursini, A. et al. From scan-to-BIM to a structural finite elements model of built heritage for dynamic simulation. *Autom. Constr.* **142**, 104518 (2022).
45. Galantucci, R. A. & Fatiguso, F. Advanced damage detection techniques in historical buildings using digital photogrammetry and 3D surface analysis. *J. Cult. Herit.* **36**, 51–62 (2019).
46. Yu, S., Zhang, D. & Qian, K. Numerical analysis of macro-scale mechanical behaviors of 3D orthogonal woven composites using a voxel-based finite element model. *Appl. Compos. Mater.* **26**, 65–83 (2019).
47. Montero-Chacón, F., Marín-Montín, J. & Medina, F. Mesomechanical characterization of porosity in cementitious composites by means of a voxel-based finite element model. *Comput. Mater. Sci.* **90**, 157–170 (2014).
48. Zhang, W. et al. Experimental study of the effect of high temperature on primary wave velocity and microstructure of limestone. *Environ. Earth Sci.* **74**, 5739–5748 (2015).
49. Song, Z., Wang, T., Wang, J., Xiao, K. & Yang, T. Uniaxial compression mechanical properties and damage constitutive model of limestone under osmotic pressure. *Int. J. Damage Mech.* **31**, 557–581, (2022).
50. Jiang, H., Jiang, A., Zhang, F. & Feng, Y. Study on creep characteristics and fractional creep damage constitutive model of limestone under thermal–mechanical action. *Int. J. Damage Mech.* **32**, 262–288 (2023).

Acknowledgements

This work was supported by the Jiangsu Province Key R&D Program Social Development Project (BE2023822), the Priority Academic Program Development of Jiangsu Higher Education Institutions (PAPD), and the project Research on the Systematic Conservation of Cultural Relics in He Garden, Yangzhou (Implementation Plan).

Author contributions

Z.H. led the research and was primarily responsible for writing the manuscript. X.Z. reconstructed the triangular grid model. Y.H. and Q.H. contributed to digital data collection. L.F. and Q.Z. reviewed and revised the manuscript. All authors read and approved the final version of the manuscript.

Competing interests

The authors declare no competing interests.

Additional information

Correspondence and requests for materials should be addressed to Qingping Zhang.